Expansion microscopy at one nanometer resolution

Ali H. Shaib[1,*], Abed Alrahman Chouaib[2], Vanessa Imani[1], Rajdeep Chowdhury[1], Svilen Veselinov Georgiev[1], Nikolaos Mougios[1,3], Mehar Monga[4], Sofiia Reshetniak[1], Daniel Mihaylov[5], Han Chen[6], Parisa Fatehbasharzad[1], Dagmar Crzan[1], Kim-Ann Saal[1], Claudia Trenkwalder[7,8], Brit Mollenhauer[8,9], Tiago F. Outeiro[10], Julia Preobraschenski[4,11], Ute Becherer[2], Tobias Moser[6,11,12], Edward S. Boyden[13], A Radu Aricescu[5], Markus Sauer[14], Felipe Opazo[1,3,15], Silvio O. Rizzoli[1,3,11,*]

[1]Institute for Neuro- and Sensory Physiology, University Medical Center Göttingen, Göttingen, Germany

[2]Department of Cellular Neurophysiology, Center for Integrative Physiology and Molecular Medicine (CIPMM), Saarland University, Homburg, Germany

[3]Center for Biostructural Imaging of Neurodegeneration, University Medical Center Göttingen, Göttingen, Germany

[4]Biochemistry of Membrane Dynamics Group, Institute for Auditory Neuroscience, University Medical Center Göttingen, Göttingen, Germany

[5]MRC Laboratory of Molecular Biology, Cambridge, UK.

[6]Institute for Auditory Neuroscience and InnerEarLab, University Medical Center Göttingen, Göttingen, Germany

[7]Department of Neurosurgery, University Medical Center, Göttingen, Germany

[8]Paracelsus-Elena-Klinik, Kassel, Germany

[9]Department of Neurology, University Medical Center, Göttingen, Germany

[10]Department of Experimental Neurodegeneration, Center for Biostructural Imaging of Neurodegeneration, University Medical Center Göttingen, 37073 Göttingen, Germany; Max Planck Institute for Multidisciplinary Sciences, 37075 Göttingen, Germany; Translational and Clinical Research Institute, Faculty of Medical Sciences, Newcastle University, NE2 4HH, United Kingdom; Scientific Employee with an Honorary Contract at German Center for Neurodegenerative Diseases (DZNE), 37075 Göttingen, Germany

[11]Cluster of Excellence "Multiscale Bioimaging: from Molecular Machines to Networks of Excitable Cells" (MBExC), University of Goettingen, Göttingen, Germany

[12]Auditory Neuroscience and Synaptic Nanophysiology Group, Max Planck Institute for Multidisciplinary Sciences, Göttingen, Germany

[13]Department of Brain and Cognitive Sciences, Massachusetts Institute of Technology, Cambridge, MA, USA; Department of Biological Engineering, Massachusetts Institute of Technology, Cambridge, MA, USA; McGovern Institute, Massachusetts Institute of Technology, Cambridge, MA, USA; Howard Hughes Medical Institute, Massachusetts Institute of Technology, Cambridge, MA, USA; Koch Institute, Massachusetts Institute of Technology, Cambridge, MA, USA; Center for Neurobiological Engineering, Massachusetts Institute of Technology, Cambridge, MA, USA.

[14]Department of Biotechnology and Biophysics, Biocenter, University of Würzburg, Am Hubland, 97074 Würzburg, Germany

[15]NanoTag Biotechnologies GmbH, Rudolf-Wissell-Straße 28a, 37079 Göttingen, Germany

*corresponding authors: ali.shaib@med.uni-goettingen.de; srizzol@gwdg.de

Abstract

Fluorescence imaging is one of the most versatile and widely-used tools in biology[1]. Although techniques to overcome the diffraction barrier were introduced more than two decades ago, and the nominal attainable resolution kept improving to reach single-digit nm[2,3], fluorescence microscopy still fails to image the morphology of single proteins or small molecular complexes, either purified or in a cellular context[4,5]. Here we report a solution to this problem, in the form of one-nanometer expansion (ONE) microscopy. We combined the 10-fold axial expansion of the specimen (1000-fold by volume) with a fluorescence fluctuation analysis[6,7] to achieve resolutions down to 1 nm or better. We have successfully applied ONE microscopy to image cultured cells, tissues, viral particles, molecular complexes and single proteins. At the cellular level, using immunostaining, our technology revealed detailed nanoscale arrangements of synaptic proteins, including a quasi-regular organisation of PSD95 clusters. At the single molecule level, upon main chain fluorescent labelling, we could visualise the shape of individual membrane and soluble proteins. Moreover, conformational changes undergone by the ~17 kDa protein calmodulin upon Ca^{2+} binding were readily observable. We could also image and classify molecular aggregates in cerebrospinal fluid samples from Parkinson's Disease (PD) patients, which represents a promising new development towards an improved PD diagnosis. ONE microscopy is compatible with conventional microscopes and can be performed with the software we provide here as a free, open-source package. This technology bridges the gap between high-resolution structural biology techniques and light microscopy, and provides a new avenue for discoveries in biology and medicine.

Introduction

Optical microscopy has been one of the most valuable tools in biology for more than two centuries, and has been considerably enhanced by the introduction of super-resolution microscopy, two decades ago[2,3]. Nevertheless, optical imaging remains difficult to perform below 10-20 nm[4,5]. Several recent works have presented localization precisions down to 1-2 nm[8-10], or even below[11], but the application of such imaging resolution to biological samples has been severely limited by two fundamental problems. First, the achievable structural resolution is determined by the labeling density, which is limited by the size of the fluorescent probes (typically 1 nanometer or larger)[12]. Second, fluorophores can interact via energy transfer at distances below 10 nm, which results in accelerated photoswitching (blinking) and photobleaching, and thus in substantially lower localization probabilities[13].

The solution to these two problems would be to separate the fluorophores spatially by the physical expansion of the specimen, in what is termed expansion microscopy (ExM[14]). To then reach the 1 nm scale, one would combine ExM with optics-based super-resolution. This has been attempted numerous times[15-22], but the resulting performance typically reached only ~10 nm. The ExM gels are dim because the fluorophores are diluted by the third power of the expansion factor, thus limiting optics techniques that prefer bright samples, as stimulated emission depletion (STED[23]), or saturated structured illumination (SIM[24]). In addition, the ExM gels need to be imaged in distilled water, since the ions in buffered solutions shield the charged moieties of the gels and diminish the expansion factor. The use of distilled water reduces the performance of techniques that rely on special buffers, as single molecule localization microscopy, SMLM[14,25] (**Extended Data Fig. 1**).

A third class of optical super-resolution approaches is based on determining the higher-order statistical analysis of temporal fluctuations measured in a movie, *e.g.* super-resolution optical fluctuation imaging (SOFI[26]) or super-resolution radial fluctuations (SRRF[6,7]). The resolution of these approaches is inversely correlated to the distance between the fluorophores and they do not require bright samples or special buffers, implying that they should benefit from ExM. To test this hypothesis, we combined X10 expansion microscopy[27,28] with SRRF[6,7,29] and established a technique we term one-nanometer expansion (ONE) microscopy (**Extended Data Fig. 1**). ONE was implemented using conventional confocal or epifluorescence microscopes and reached 1 nm or better resolutions across different samples and color channels. To aid in its implementation, we generated a ONE software platform, as a plug-in for the popular freeware ImageJ (Fiji) (**Supplementary Fig. 1**; Supplementary Software).

Principles and validation of ONE microscopy

We first attached a gel-compatible anchor (Acryloyl-X) to protein molecules, either purified or in a cellular context, and then embedded these samples into a swellable

X10 gel[27,28]. Proteins were hydrolysed by proteinase K or by heating in alkaline buffers, leading to main chain breaks. This enables a highly-isotropic 10-fold expansion of the sample, which is achieved by distilled water incubations[27,28]. We then imaged the samples using wide-field epifluorescence or confocal microscopy, acquiring series of images (movies) of hundreds to thousands of images (ideally 1500-2000) in which the fluorescence intensity of the fluorophores fluctuates (**Extended Data Fig. 2**). Each pixel of a frame was then magnified into a large number of subpixels, and the local radial symmetries of the frame (which are due to the radial symmetry of the microscope's point-spread-function, PSF) were measured. This parameter, termed "radiality" was analyzed throughout the image stack, by higher-order temporal statistics, to provide the final, fully resolved image[6,7,29].

In theory, the precision of the SRRF technique should reach values close to 10 nm[6]. In practice, it has been limited to resolutions of ~50-70 nm, because the radiality of biological samples is reduced by the presence of overlapping fluorophores. A second limitation is the signal-to-noise ratio, which is strongly correlated to the radiality performance. These limitations were alleviated by ExM. The distance between the fluorophores increases, enabling the study of intensity fluctuations from individual dye molecules independently. The signal-to-noise ratio also increased, even for idealized samples consisting only of fluorescently-conjugated nanobodies in solution (**Extended Data Fig. 3**). This approach should therefore allow a SRRF performance down to ~10 nm which, divided by the expansion factor, represents a ~1 nm practical resolution (**Extended Data Fig. 1b**), as long as the gel expands isotropically in all dimensions. The X10 gel, based on *N,N*-dimethylacrylamide acid (DMAA), rather than the acrylamide used in typical ExM protocols, has a more homogeneous distribution of cross-links[30], thus leading to fewer errors in expansion (see[31] for a further discussion on gel homogeneity).

To assess the performance of ONE microscopy in a cellular context, we first analysed microtubules, the a standard reference structure in super-resolution imaging techniques[17]. Gels were stabilized in specially-designed imaging chambers (**Supplementary Fig. 2**), which enabled high-quality images of the antibody-decorated microtubules at both 10-fold and ~3.5-fold expansion (the ZOOM ExM technique[32] was used for the latter; **Fig. 1**). To determine the ONE microscopy resolution, we performed a Fourier Ring Correlation (FRC)[33] analysis. The maximal resolution values, reported as customary in the super-resolution field[34], were around 0.8-1 nm (**Extended Data Fig. 4**). The microtubule sizes matched previous measurements[35,36], ~60 nm in diameter, when labelled with secondary antibodies, and around 30-35 nm, when labelled with secondary nanobodies (**Extended Data Fig. 4e,f**).

We then evaluated a purified ALFA-tagged EGFP construct bound simultaneously by two anti-GFP nanobodies[37] and by an anti-ALFA nanobody[38]. This results in a triangular semi-flexible arrangement, which we termed a "triangulate smart ruler" (TSR, **Fig. 1b; Extended Data Fig. 5**). The TSR aspect observed in ONE microscopy is consistent with crystal structures of nanobody-EGFP and nanobody-ALFA complexes (**Fig. 1b,c**).

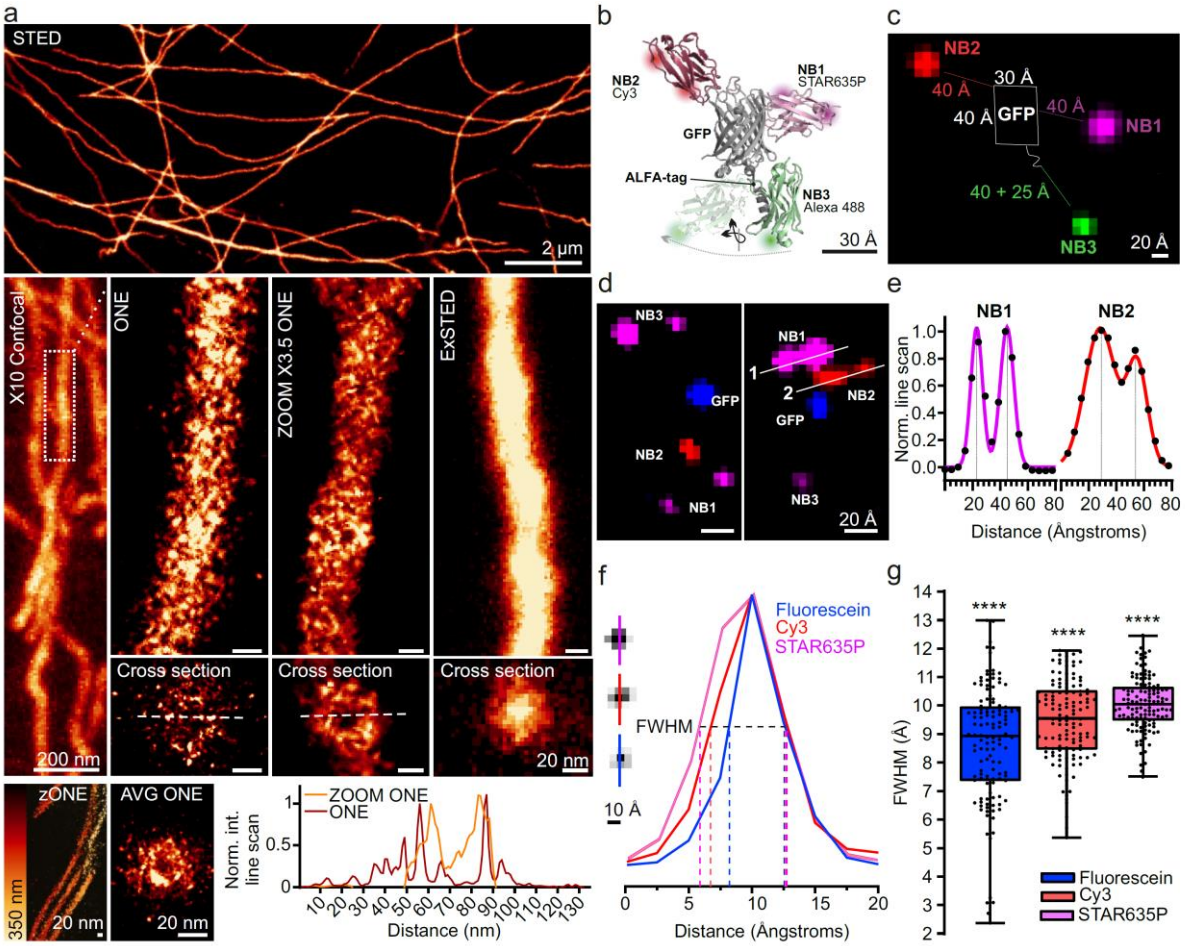

Figure 1. One nanometer resolution in biological samples. a, Tubulin immunostainings (relying on primary and secondary antibodies) imaged using STED, without expansion (top), confocal after X10 expansion, ONE microscopy, ONE with ZOOM ExM (3.5-fold), and STED with X10 expansion (ExSTED). Bottom left, ONE microscopy images at different Z-axis levels, obtained by confocal scanning at different heights (zONE). Bottom middle (AVG ONE) shows an average of 36 cross-sections. The graph depicts the line scans indicated by the dashed lines. **b**, The general scheme of the GFP-based assemblies (generated in Pymol, using the PDB structures 6I2G and 3K1K). **c**, Typical ONE microscopy image, with the rough positioning of the molecules indicated by the cartoon. The three nanobodies carry three spectrally different fluorophores. **d**, Two further examples, relying on a design in which NB1 and NB3 carry identical fluorophores. To detect GFP, the samples were labeled with NHS-ester fluorescein, after homogenization. Here we used a small pixel size, enabling the detection of two fluorophores connected to the nanobodies (see Supplementary Figure 3). **e**, Line scans across the dual fluorophores indicated in panel d. **f**, To approximate the resolution of the system, we drew line scans across spots and measured the full width at half maximum (FWHM) in curve fits executed on the line scans. **g**, FWHM 129, 135, and 132 fluorescein, Cy3 and STAR635P line scans. The values are significantly different between the color channels. $p < 0.0001$, Kruskal-Wallis test. The box plot shows the median, 25th percentile and the range of values.

To reveal the protein molecules themselves (the 10-fold expansion eliminates the endogenous GFP fluorescence for example), we labeled the TSRs using NHS-ester fluorescein[39,40]. This is possible because proteins are broken during homogenization at multiple main chain positions, and each resulting peptide has an exposed amino terminal group that can be efficiently conjugated with N-hydroxysuccinimide ester (NHS-ester) functionalized fluorophores. It is known that nanobodies are not as strongly anchored to ExM gels as other proteins, owing to their low lysine content, and

most of their peptides are lost[17]. Their fluorescein signal is therefore poorer than that of GFP (**Fig. 1d**). This is an unexpected bonus in ONE microscopy experiments because nanobody signals do not obscure those resulting from the protein of interest (see Supplementary Fig. 3 for a gallery of examples). In these experiments we used a smaller pixel size than in Fig. 1c (0.48 nm vs. 0.98 nm), which enabled us to often observe dual fluorophores, in agreement with the fact that these nanobodies can be labelled at two positions (**Fig. 1b, d**). The distances between the two fluorophores on one nanobody (**Fig. 1e**) are consistent with the size of nanobody molecules (**Fig. 1b**). Measuring the full width at half-maximum (FWHM) of the fluorescence signals suggest a resolution of 0.85-1 nm in the different fluorescence signals, including the fluorescein channel (**Fig. 1f,g**), similar to the respective FRC analysis results (**Extended Data Fig. 5**).

ONE microscopy can reveal protein shapes

Considering the high resolution attainable and the fact that proteins expand 1000x in volume but fluorophores do not, we hypothesized that our NHS-ester labelling method could be optimized to enable the analysis of protein shapes by ONE microscopy. We first applied this approach to antibody molecules, and we could observe immediately recognizable outlines for IgGs, IgAs and IgMs (**Fig. 2a-c, Supplementary Fig. 4**). Fluorescent labels attached to of secondary IgG antibodies could also be observed in the same images (**Fig. 2a; Supplementary Fig. 4**) and also in complexes between fluorescently-conjugated primary and secondary antibodies, or nanobodies (**Fig. 2d**). We applied the same labelling method to a membrane protein, the full-length β3 human γ-aminobutyric acid ($GABA_A$) receptor homopentamer, a ligand-gated chloride channel[41]. “Top” (extracellular, revealing the receptor vestibule), side and “bottom” (intracellular) views could be readily observed in single particles based on similarity with the crystallography and single-particle cryogenic electron microscopy (cryo-EM) structures (**Fig. 2e; Supplementary Fig. 5**). It is worth noting that particles observed by ONE microscopy are indeed single molecules, and no averaging or classification has been performed on these datasets. The side views seem to reveal additional signals from the long M3-M4 loops, not visible in crystal or cryo-EM structures due to truncations or disorder[41,42], but labelled by NHS-fluorescein.

We next investigated a protein of unknown structure, the ~225 kDa otoferlin, a Ca^{2+} sensor molecule that is essential for synaptic sound encoding[43]. The outlines provided by ONE microscopy imaging strongly resemble the AlphaFold[44] prediction for this protein (**Fig. 2f,g, Supplementary Fig. 5**). Moreover, scanning in both the axial and lateral dimensions, using confocal laser scanning microscopy, enabled us to obtain 3D information on single otoferlin molecules (**Fig. 2h**). At the opposite end of the Ca^{2+} sensor size spectrum, we sought to visualize the small (~17 kDa) protein calmodulin. To our surprise, even for such small particles, it was possible to observe dynamic changes in their shape upon Ca^{2+} binding (**Fig. 2i-l**).

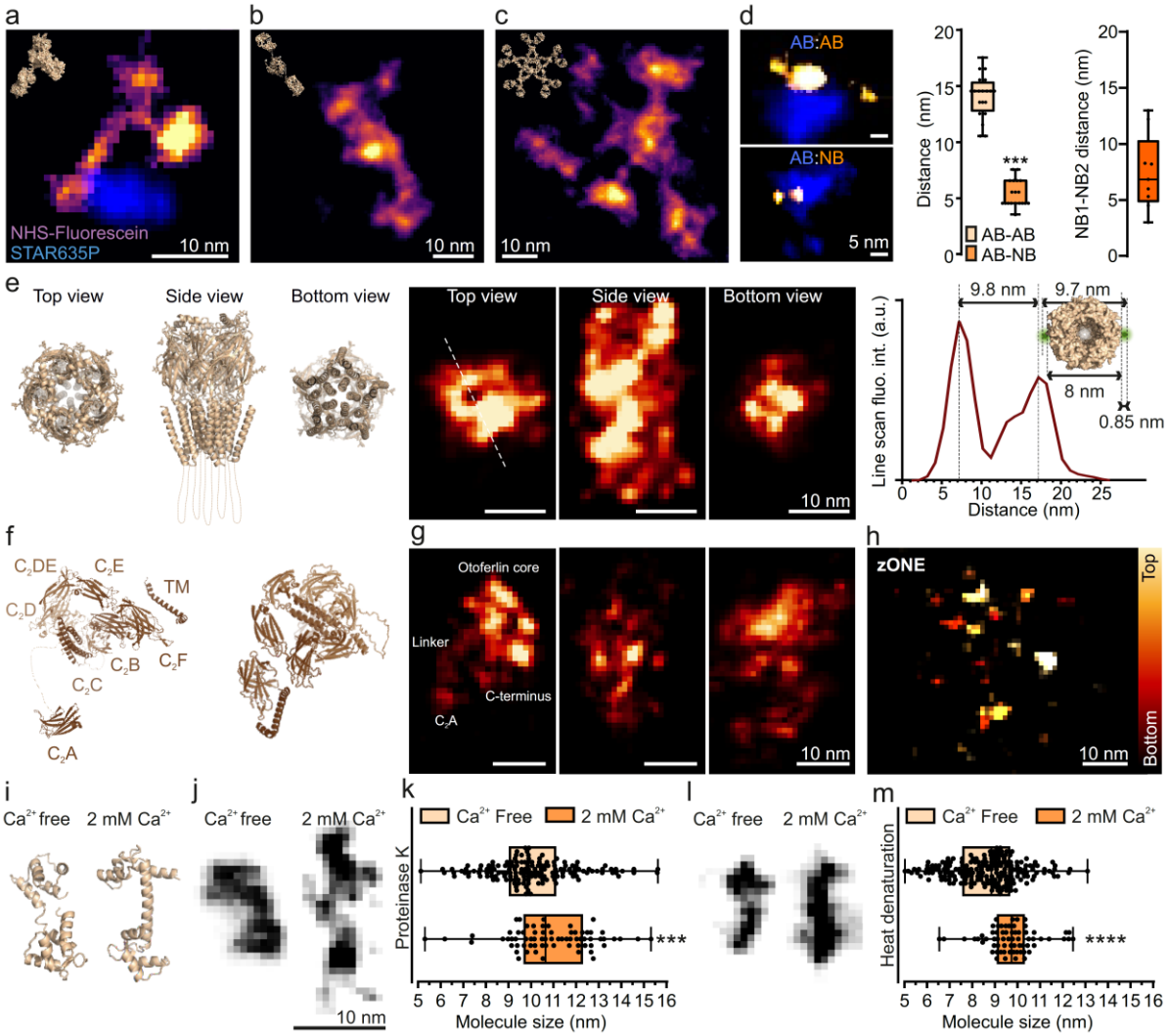

Figure 2. ONE analysis of single molecules. a-c, Images of isolated immunoglobulins (IgG, IgA, IgM), labeled with NHS-ester fluorescein after homogenization. The IgGs were secondary anti-mouse antibodies, carrying STAR635P (blue). **d**, Distances between fluorescently-conjugated IgGs and fluorescently-conjugated secondary antibodies (top) or secondary nanobodies (bottom). In panels a-d we used a different fluctuation analysis, termed temporal radiality pairwise product mean, TRPPM, unlike the temporal radiality auto-cumulant to the order of 4 (TRAC4)[6] approach used in most other figures. Unlike TRAC4, which aims to separate the individual fluorophores, TRPPM enhances the cohesiveness of the fluorophores decorating the single antibodies, resulting in cloud-like signals whose distances are easily measured (N = 20/19, for AB:AB/AB:NB). Right panel: distance between the two secondary nanobodies binding single IgGs (N = 9). **e**, A similar analysis of purified $GABA_A$ receptors. Line scans across specific profiles seem to detect the receptor pore. **f**, AlphaFold-derived structure of otoferlin. **g**, ONE examples of otoferlin images. **h**, Z-axis ONE imaging, indicating that two components (presumably C_2A and TM domains) are relatively far from the main body of the molecule. **i**, PDB structures of the Ca^{2+} sensor calmodulin, in presence or absence of its ligand, along with ONE images, after proteinase K-based homogenization and expansion (see Supplementary Fig. 6 for more images). **j**, The expected elongation by ~1 nm was reproduced (p = 0.0006, Mann-Whitney test; N = 70-155). **k-l**, Similar analysis, after homogenization using autoclaving (p <0001, N = 66-197). The box plot shows the medians, the 25th percentile and the range of values.

Visualization of synaptic proteins

We next tested the performance of ONE microscopy in cultured neurons, focusing on the synaptic transmission machinery. Synaptic vesicles fuse to the plasma membrane to release their neurotransmitter contents, and their molecules are afterwards endocytosed, following different pathways[45]. A significant fraction of the vesicle proteins are found on the plasma membrane, forming the so-called "readily retrievable pool"[46]. It is unclear whether these proteins are grouped in vesicle-sized patches, or whether they are dispersed on the presynaptic membrane. We investigated this here, using a fluorescently-conjugated antibody directed against the intravesicular domain of the Ca^{2+} sensor synaptotagmin 1 (Syt1), an essential component of the vesicles. The labeling density was sufficiently high to reveal that endocytosed vesicles have the expected circular shape (**Fig. 3a**). Turning to the readily retrievable pool, we found that the molecules were grouped in areas consistent with theoretical expectations for fused vesicles, with copy numbers similar to the values expected for this molecule (7-15 per vesicle[47,48]) taking into account the fact that one antibody can bind two synaptotagmin 1 molecules (**Fig. 3b,c**). Removing cholesterol from the plasma membrane forced the dispersion of synaptotagmin molecules (**Fig. 3b,c**), albeit it left the overall synapse organization unaffected (**Supplementary Fig. 7**).

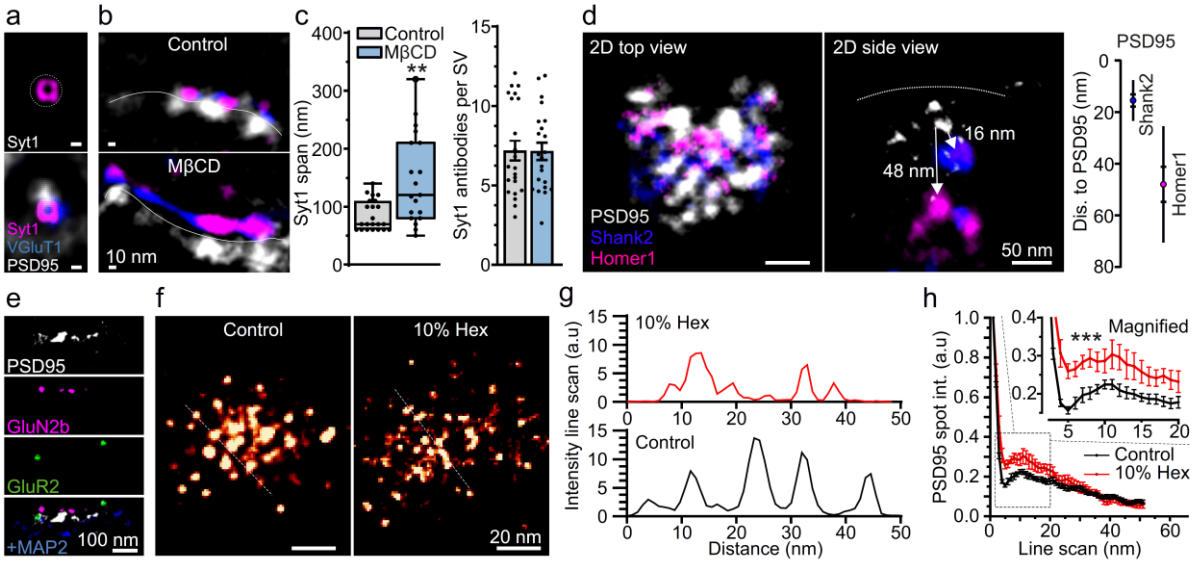

Figure 3. ONE reveals pre- and postsynaptic structures. a-c, Synaptic vesicles were labeled live using an antibody against a luminal epitope of synaptotagmin 1 (Syt1, magenta). The vesicular glutamate transporter (vGluT1, blue) and PSD95 (gray) were immunostained using an antibody and a nanobody, respectively. **a**, Recently endocytosed vesicle exhibiting circular morphology. **b**, Readily retrievable pool molecules form patches containing Syt1/vGluT1 (top), which are dispersed by cholesterol extraction using MβCD (bottom). **c**, MβCD causes molecules to spread across larger areas (left: N = 22-19, 2 independent experiments, $p < 0.0044$, Mann-Whitney test; right: N = 22-22, 2 independent experiments, $p = 0.8937$), although the signal per vesicle (the Syt1 copy number) remains unchanged. **d**, A visualization of PSDs (top and side views), after immunostaining PSD95 with the same nanobody used in a-c, and Shank2 and Homer1 with specific antibodies. The graph indicates the axial positioning, which agrees well with the literature[49]. N = 11 measurements for each protein, 2 independent experiments; symbols show the medians, SEM and SD. **e**, Side view of a postsynapse displaying PSD95, MAP2 and two glutamate receptors (GluR2, AMPA type, and GluN2b, NMDA type). **f**, ONE images of PSD95 (top views), before or after the addition of 10% 1,6-hexanediol (Hex). **g**, Line scans through the PSD95 stainings shown in panel f. **h**, An analysis of PSD95 spot profiles; N = 10-7

synapses, Friedman test followed by Dunn-Sidak testing, $p = 0.0027$; the error bars show the SEM. For details on the analysis, see Supplementary Fig. 8.

In the post-synaptic compartment, we could confirm known organization principles, including the layered aspect of the postsynaptic density (PSD), in which molecules like PSD95, Shank and Homer occupy different positions in the axial direction (**Fig. 3d**), or the clustered distribution of postsynaptic receptors, with NMDA receptors typically observed in more central locations than AMPA receptors (**Fig. 3e;** see also [50]). These experiments confirm the ease with which ONE microscopy provides multicolor super-resolution in crowded cellular compartments.

PSD95 has a retiolum-like organization

The fine structure of the PSD, or even its very existence, is a matter of considerable debate. The current prevalent view is that the PSD is maintained by liquid-liquid phase separation (LLPS)[51], which, intuitively, implies an amorphous organization. To test this hypothesis, we immunostained PSD95 in hippocampal cultured neurons, using a specific nanobody (**Fig. 3f**). PSD95 appears to be organized in a quasiregular lattice, a conclusion that was strengthened by overlaying PSD images to obtain average views (**Extended Data Fig. 6**). An analysis of the distances between PSD95 spots revealed that they have a preferred spacing of ~8-9 nm, which is significantly different from a random distribution (**Extended Data Fig. 7**). A similar result was obtained when using a Ripley curve-like analysis (**Fig. 3g,h**; see **Supplementary Fig. 8** for details). To test the stability of the supramolecular PSD95 arrangements observed, we incubated the cells with 1,6-hexanediol, an alcohol that has been often used to cause the dispersion of liquid phases[52]. This treatment readily dispersed other components of the PSD, as Homer1 and Shank2, but did not affect PSD95, which appeared to remain unchanged at the confocal imaging level (**Extended Data Fig. 7d**). This was no longer the case when samples imaged in ONE microscopy, as the 1,6-hexanediol treatment caused the PSD95 arrangements to lose much of their regularity (**Fig. 3f-h**).

These results suggest that the PSD95 positioning may only be partially, but not fully, controlled by LLPS mechanisms. We propose the term "*retiolum*" for this nanoscale PSD patterning, a Latin term describing small string nets with knots at regular intervals[53]. These fine details of PSD95 organisation are fundamentally different to the PSD95 nanodomains observed in the past by super-resolution imaging of antibody-based immunostaining[50,54]. The nanodomains observed in the past are most likely a result of the limited resolution of the respective technologies, as demonstrated in **Extended Data Fig. 8**.

While all of the results presented above on synaptic proteins were derived from neuronal cell cultures, we would like to point out that ONE microscopy can also be

applied to tissue samples to investigate such protein arrangements, as we performed for brain slices of more than 200 µm in thickness (**Extended Data Fig. 9**).

Towards Parkinson's Disease diagnostics

We next sought to address a pathology-relevant imaging challenge by ONE microscopy. Parkinson's disease (PD) is a neurodegenerative disease characterized by the accumulation of aggregates composed of several proteins, of which alpha-synuclein (ASYN) is the most prominent[55]. ASYN can exist as a monomer, or assemble into different species, such as soluble oligomers and fibrils (e.g.[56]). ASYN in patient samples such as cerebrospinal fluid (CSF) is a realistic target for PD diagnostic studies, albeit results based on measuring its concentration have limited diagnostic success[57-59].

We explored the diagnostic potential of imaging ASYN assemblies in the CSF of PD patients *versus* controls (**Supp. Table 1**). A nanobody[60] was used because full-length immunoglobulins only provide relatively poor labeling due to their large size (**Fig. 4a, Supplementary Fig. 9**). Different types of ASYN assemblies could be revealed (**Fig 4b**) and PD patients had higher levels of oligomer-like structures (**Fig. 4c,d**).

We classified the structures observed and noticed that the "very large" assemblies (>200 nm in length, >50 nm in width) were found at similar frequency in PD patients and controls (**Fig. 4e**). The same was observed for assemblies in the 50 to 200 nm length range (**Fig. 4e**). However, this was not the case for the smaller, oligomer-like assemblies. Some resembled strikingly polymorphic ASYN assemblies that have been recently described by cryo-EM[61,62], while others had an annular organization as observed in the past by negative stain transmission EM or cryo-EM [63,64]. All oligomer-like species were significantly more abundant in PD than in controls (**Fig. 4f**), and their cumulative analysis, which alleviates ambiguities due to imperfect classification, resulted in a good discrimination of PD patients and age-matched controls (**Fig. 4g,h**; for overviews of more ASYN objects see **Extended Data Fig. 10**). We conclude that the analysis of ASYN aggregates is a promising procedure for PD diagnosis.

Finally, ONE can also analyze medical samples that have been fixed for prolonged (and uncontrolled) time periods, as observed for chemically fixed blood sera from COVID-19 patients, obtained commercially (**Supplementary Fig. 10**). Here we observed that the patient IgGs clustered in specific regions of the viral particles, whose detailed composition could be targeted in the future.

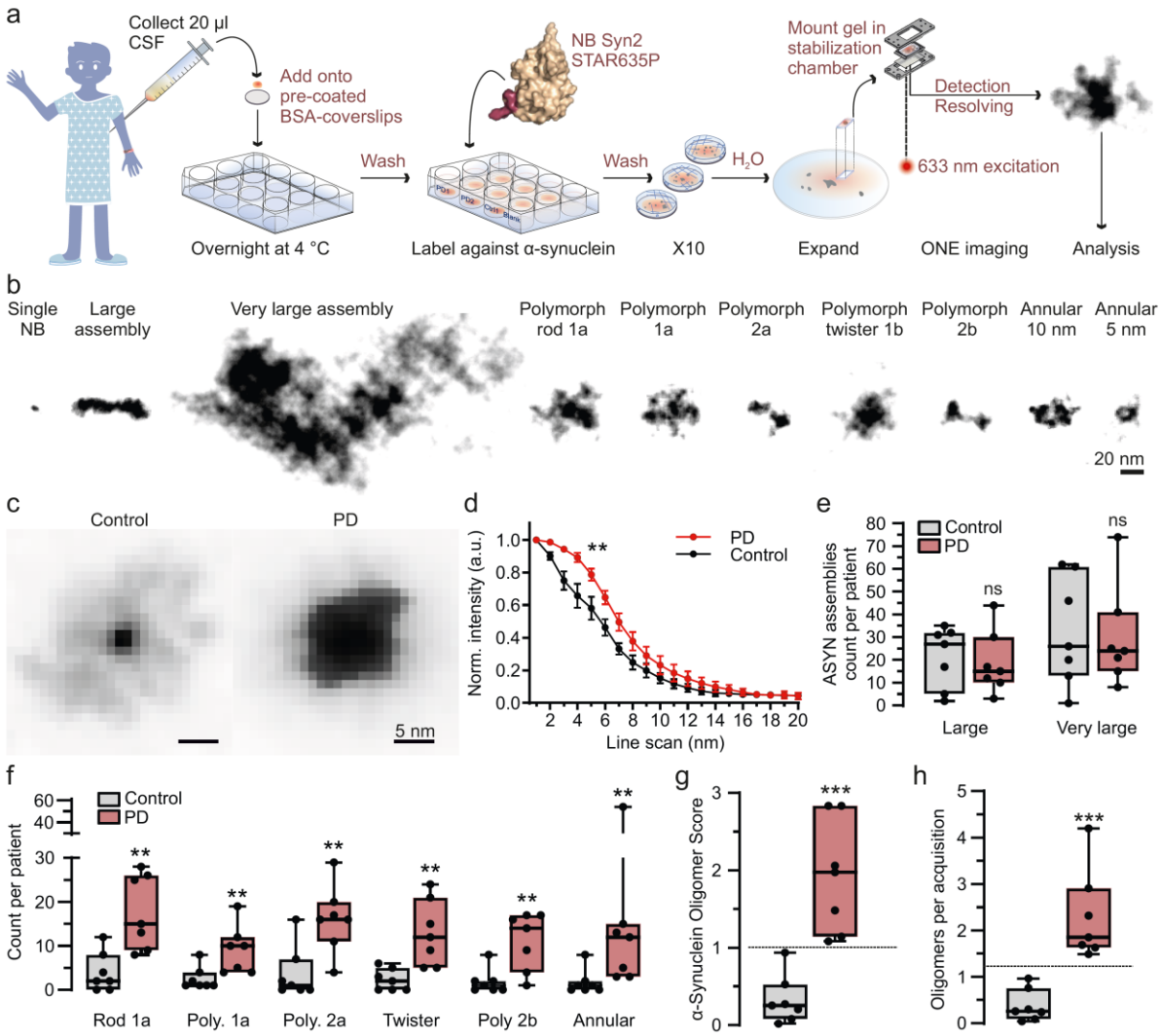

Figure 4. A promising avenue for Parkinson's Disease (PD) diagnostics. a, Cerebro-spinal fluid probes were obtained from PD patients and controls, and 20 µl amounts were placed on BSA-coated coverslips, followed by ONE imaging, after immunolabeling ASYN using a specific nanobody[60]. **b**, A gallery of typical ASYN species observed in the CSF samples. **c**, Average ASYN assemblies from a PD patient and a control. **d**, An analysis of the spot profiles detects significant differences, with the average control object being smaller than the average PD object. All ASYN assemblies for the control and PD patients were averaged, from 3 independent experiments, Friedman test followed by Dunn-Sidak, $p = 0.0237$; errors show SEM. **e**, An analysis of the numbers of the larger assemblies in CSF samples. No significant differences, Mann-Whitney tests, $p = 1$, $p = 0.7104$. **f**, An analysis of the numbers of oligomers in CSF samples. All comparisons indicated significant differences, Mann-Whitney tests followed by a Benjamini-Hochberg multiple testing correction with FDR of 2.5%; p values = 0.0105, 0.0023, 0.0111, 0.0012, and 0.0012, in the respective order of data sets. **g**, Analyses of the numbers of oligomers, as a proportion of all ASYN assemblies analyzed (left), or as numbers per acquisition in (**h**). Both procedures discriminate fully between the PD patients and the controls. For the second procedure, the lowest PD value is 50% larger than the highest control. N = 7 PD patients and 7 controls, Mann-Whitney test, $p<0.0001$ for both **h** and **g**.

Discussion

Here we show that a fluorescence microscopy procedure based on a combination of X10 ExM and radial and temporal fluorescence fluctuation analysis (SRRF) can provide a spatial resolution of ≤ 1 nm. In practical terms, most of the data presented here have been acquired with a standard, ~15 years old, confocal microscope. Therefore, ONE microscopy makes super-resolution imaging broadly available, in a fashion that has always been a primary goal of ExM[65]. Moreover, no special handling, unusual fluorophores or reagents are necessary. We provide a free, open-source software package for this. The ONE data processing is relatively fast because the SRRF procedure is performed in minutes. The initial immunostaining and expansion procedures take, combined, 3-4 days, while imaging individual regions of interest only takes between 35 seconds and 2 minutes, depending on the number of color channels.

The ONE axial resolution surpasses that of confocal microscopy by one order of magnitude, owing to the 10x expansion factor. Further improvements of axial resolution could be introduced in the future, through total internal reflection fluorescence (TIRF), lattice light-sheet microscopy[66], or multi-focus microscopy[7]. The only major limitation we see is that ONE cannot be applied to live samples, due to the ExM procedures. Therefore, the MINFLUX concept[8,11,67,68] is currently the only solution for live imaging at resolutions ≤5 nm. Nevertheless, future developments in ONE microscopy are likely to enable 3D structural analysis of proteins, either purified or in cells and tissue samples, at resolutions approaching electron cryo-microscopy and tomography techniques, at room temperature and at a fraction of the cost. Developments envisaged include a refined anchoring chemistry of proteins into the gel structure, development of gels that are homogeneous to sub-nanometer levels, as well as imaging automation, to enable the analysis of tens of thousands of particles in a time-efficient manner.

Overall, we conclude that the ONE technology provides a simple, robust and easily applied technique for the investigation of the domain beyond super-resolution, which could be termed ultra-resolution, bridging the gap to X-ray crystallography and electron microscopy-based technologies.

Extended Data Figure legends

Extended Data Fig. 1. A general overview of the ONE microscopy approach. a, Biological samples are linked to gel anchors, relying on Acryloyl-X, followed by X10 gel formation and homogenization, either by proteinase K additions or by autoclaving in alkaline buffers. Full expansion is achieved by repeated washes, and is followed by mounting gel portions in a specially designed chamber. In principle, one could image the samples using different super-resolution procedures. Techniques benefitting from bright samples, as STED or SIM, suffer due to the fluorophore dilution induced by the expansion procedure. Techniques requiring special buffers (*e.g.* SMLM) are negatively affected by the water environment. In contrast, technologies relying on fluorophore fluctuations profit from the expansion, as the fluorophores are spatially separated and can fluctuate independently. **b**, Repeated imaging is performed (up to 3000 images), in any desired imaging system (confocal, epifluorescence, etc.), to detect signal fluctuations, which are then computed using through a plugin (ONE platform) based on the SRRF algorithm, before assembling the final super-resolved images.

Extended Data Fig. 2. A detailed view of the ONE procedure. a, Processing a stack of diffraction-limited images with SRRF, based on the analysis of a gradient of convergence of sub-pixels over a radiality stack, results in super-resolved images with resolutions varying between 50-70 nm. **b**, The ONE procedure adapts the SRRF algorithm to expanded gels. **c-f**, A detailed explanation of the analysis procedure. **c**, A sample was fixed and expanded using a 10-fold expansion protocol (X10). The sample was then imaged using a resonant scanner on a confocal microscope. The zoomed-in view indicates one bright spot, whose size in real space is limited by diffraction to ~200-300 nm, but represents a 10-fold smaller size in the pre-expansion space (see scale bars in the middle panels). Every pixel is then subjected to a 10-fold radiality magnification and is then subjected to the procedure explained in panels d-f, which provides the final, high-resolution image (right-most panel). **d**, Signal fluctuations are measured by imaging the sample repeatedly, using the resonant scanner (here at 8 kHz). **e**, A view of the overall signals, obtained by summing 20 of the fluctuating images (raw in the left-most panel, background-subtracted in the middle panel), or by summing 1000 images. **f**, Each image from series obtained as in panel b is subjected to a temporal analysis of fluctuating fluorophores, based on radiality magnification[6], thereby providing a super-resolved image whose level of detail becomes optimal after ~1500 frames.

Extended Data Fig. 3. Expansion microscopy results in a higher signal-to-noise ratio. Expansion microscopy, which separates proteins of interest and removes much of the other cellular components (*e.g.* lipids, metabolites) should result in a higher signal-to-noise ratio (SNR). **a**, To test this, we analyzed here the simplest possible sample, consisting of Star635P-conjugated nanobodies on glass coverslips, or in expanded gels, using confocal microscopy, relying on analysis using a resonant scanner. **b**, The SNR of these samples increases by 2-fold, on average, after expansion. N = 30-24, $P = 0.000001$, Mann-Whitney Ranksum test.

Extended Data Fig. 4. The ONE resolution reaches sub-nanometer values in tubulin immunostainings. a, An analysis of tubulin, following immunostainings relying on primary antibodies detected using Star635P-conjugated secondary nanobodies. While the overall signal distribution is similar to that obtained with secondary antibodies (Fig. 1), one can observe often pairs of fluorescent spots in very close vicinity (marked by dotted circles in the cross section), which probably represent the two fluorophores on each nanobody. For a formal analysis of this issue on different nanobodies, see Fig. 1 and Extended Data Fig. 5. **b**, A Fourier Ring Correlation (FRC) analysis of a tubulin immunostaining. The best resolution obtained is ~0.8 nm. **c**, The best resolution obtained per image (N = 5 analyses). **d**, The average resolution obtained per image (N = 5 analyses). **e**, Immunostainings relying on primary antibodies followed by secondary antibodies (upper panel) or by secondary nanobodies (lower panel). **f**, The graph shows the diameter of microtubules in when using secondary antibodies (left; N = 49 microtubule profiles) or secondary nanobodies (right; N = 101).

Extended Data Fig. 5. In-depth analysis of GFP-nanobody complexes. a, Dot blots to validate that each nanobody was binding specifically the TSR individually. Nitrocellulose membranes were spotted with TSRs and bovine serum albumin, as control, and the spots were revealed with the respective nanobodies. **b**, An overview of an image showcasing nanobodies bound to their GFP target. **c**, An analysis of distances from STAR635P to Cy3 nanobodies, in normal images or after mirroring one of the fluorescence channels, as a negative controls. The close-distance interval is largely removed by mirroring. N = 40-40 TSRs. Performing this in samples lacking the GFP, in which the nanobodies are randomly distributed, results in no differences between the normal and mirrored distributions. N= 40/40 images. **d**, Overview of the TSR using only two-color nanobody labeling (same as the one used in Fig. 5c,d), along with two different examples. The sample is also labeled using NHS-ester fluorescein, and a small pixel size (0.48 nm) is used, to enable the optimal visualization of the TSRs. **e**, An analysis of the signal-to-noise ratio of the TSRs, obtained by measuring the noise levels in the vicinity of the nanobodies. The noise levels are normalized to 1, implying that the normalized signal of the respective nanobodies now provides directly the signal-to-noise ratio. N = 20-18, 12-14, and 17-11 measurements, $P < 0.0001$, Mann-Whitney test. **f**, A Fourier Ring Correlation (FRC) analysis of nanobody images. The best resolution obtained is ~1 nm. **g**, The best resolution obtained per image, in the different color channels (N = 5 analyses).

Extended Data Fig. 6. Further PSD examples. a, ONE imaging of PSDs, employing a resonant scanner and a final pixel size of 1 nm, achieving high resolution (same procedure and resolution as in Fig. 3f). **b**, Examples of PSD95 stainings, after treatment with 1,6-hexanediol (Hex), as in Fig. 3f. **c**, We averaged the PSD95 signals for both control and Hex-treated synapses (8 PSDs imaged in top views, for each treatment). The control shows a somewhat regular pattern, while the Hex treatment seems to perturb this.

Extended Data Fig. 7. A detailed analysis of the PSD. a, The PSD was immunostained for PSD95, Homer1 and Shank2, as in Fig. 3, and images were taken at different heights along the Z-axis (zONE imaging). An overlay (summed image) is shown in the left panel, along with an analysis of the proteins at different Z levels, using a colormap that describes the positions along the Z axis (right panel). **b**, The distance between PSD95 spots was computed from images as in panel a, and was compared to that obtained from positioning the molecules randomly within the PSD95, N = 10 synapses, Friedman test followed by Dunn-Sidak, p=0.0001. **c**, The lateral distance between PSD95 spots and between PSD95 and Homer1 or Shank2. The minimal distance between each PSD95 spot and a Homer1/Shank2 spot is shown (measured in the lateral plane, in 2D projections of the PSD). N = 10 synapses, from 2 independent experiments. While the distance between PSD95 spots has a non-random character, as indicated in panel b, the distances to Homer1 or Shank2 spots are not different from randomized distributions (Dunn-Sidak tests, p>0.1), possibly also because these two molecules are immunostained using antibodies, which causes the fluorescence signals to scatter broadly. **d**, Confocal microscopy analysis of the PSDs, in non-expanded samples. In control conditions all three components analyzed here (PSD95, Homer1, Shank2) are well colocalized. The addition of 3% 1,6-hexanediol (Hex) causes the dispersion of Homer1 (magenta), while 10% Hex also disperses Shank2 (blue). PSD95 remains largely unaffected by Hex. **e**, An analysis of the average PSD95 spot profile confirms this impression, N = 10-7-10 neurons, a set from 3 independent experiments. **f**, We analyzed the dispersion of Homer1 (left) and Shank2 (right) away from the PSD95 spots. The signal present in synapses (near the PSD95 labeling, but not within the PSD) was analyzed, to determine the % that is not correlating to the PSD structure. The same samples were analyzed as in panel e.

Extended Data Fig. 8. ExM-STED (ExSTED) imaging of PSDs. a, Hippocampal cultures were immunostained for PSD95 and VGlut1, and were additionally labeled with NHS-ester fluorescein, after homogenization. **b**, A gallery of high-zoom ExM-STED views of synapses, with a focus on PSD95. Relatively large PSD domains are visible, as in most previous works in the literature, and unlike most of our ONE images. **c**, To determine if this is simply an issue of resolution, we aimed to generate ExM-STED-like images with ONE microscopy, by reducing its resolution. We employed an epifluorescence microscope (as opposed to a rapidly scanning confocal in the panels dealing with PSD95 in Fig. 3), and

we used the temporal radiality pairwise product mean (TRPPM) option of analysis, which broadens the resulting spots. The results are very similar to ExM-STED images, demonstrating that the modular/domain appearance of the PSD95 stainings is a result of insufficient resolution, with a *retiolum* being evident only at very high resolution (under optimal ONE imaging).

Extended Data Fig. 9. ONE analysis of brain slices. a, Images of a 200 µm-thick rat brain section before (left) and after (right) expansion, relying on autoclaving for homogenization[69]. The scale bar does not take the expansion factor into consideration. The sections were labeled by using NHS-ester fluorescein incubations. **b**, Epifluorescence images of expanded brain slices, focusing on Bassoon and Homer1 as pre- and postsynaptic markers, respectively. **c**, Similar images, taken using the ONE procedure. **d**, Line scans executed over the areas indicated in panels b and c. As expected, far more detail can be observed in ONE than in simple epifluorescence microscopy.

Extended Data Fig. 10. A gallery of ASYN object images from 7 PD patients and 7 controls. The images were obtained following the procedure indicated in Fig. 4a. See Supp. Table 1 for details on the respective patients.

Supplementary Figure legends

Supplementary Fig. 1. ONE analysis and examples. a & **b**, Several views of the starting interface of the ONE software package. The examples show the intuitive software choices. See also the "Readme/Help" file of the software package. **c**, Examples of different potential artifacts that should be avoided in ONE imaging. **d**, Different potential choices in how to resolve ONE images. We suggest using the temporal radiality pairwise product mean (TRPPM) procedure for dim samples. This reduces the obtainable resolution, but follows much better the potential sample shape. For brightly labeled samples with direct labeling, the temporal radiality auto-cumulant (TRAC4) procedure provides the best resolution and SNR, indicating the positions of the individual fluorophores.

Supplementary Fig. 2. Technical scheme of the stabilization chamber used in this work. The exact measurements and materials for the stabilization chamber are included in the figure text. The 3D-printed gel cage patterning can be organized according to the user's preferred design. Only a suggested design is included here (many others work equally well).

Supplementary Fig. 3. TSR gallery. a, An example of a TSR. The first panel shows a ONE image of a TSR, the middle panels shows a cartoon model that fits the imaged TSR, and the third panel shows an overlay of the ONE image and the model. **b**, A gallery of TSRs (upper panels) and a best guess of cartoon models overlaid over the TSR images (lower panels).

Supplementary Fig. 4. Further ONE examples of immunoglobulin imaging. a, An overview of a field showing IgG antibodies labeled using NHS-fluorescein (left), along with a few zoom-in images of fluorescently-conjugated secondary IgG antibodies (right; Abberior Star635P conjugation shown in blue). **b**, Several examples of IgG antibodies imaged in different positions and perspectives. **c**, A gallery of the expected antibody shapes, obtained by convoluting a PDB IgG structure with a ONE point-spread-function, after revolving the IgG molecules in 3D space randomly. A few enlarged views are shown, along with a multitude of small-sized views, to explain how IgG molecules should appear when they are visualized in fluorescence in random orientations. The typical IgG views are similar to the modeled ones. **d**, Fluorescence (Abberior Star635P) and Coomassie SDS-PAGE gels indicating the size distribution of antibody fragments. A mouse monoclonal primary antibody was run on the gels, along the secondary antibody imaged in panel a. The gel was first imaged under a fluorescence (Cy5 channel) and then total proteins were revealed with Coomassie brilliant blue staining. The results suggest that numerous small fragments are expected for both primary and secondary antibodies in the ONE images, not only full antibodies, due to impurities being present in the commercial antibody samples. **e-f**, An overview of IgA molecules. **g-h**, A similar overview of IgM molecules. The antibody structures are shown using Pymol representations from PDB structures 1HZH, 1IGA, and 2RCJ.

Supplementary Fig. 5. $GABA_A$ receptor and otoferlin galleries. a, An overview of images of $GABA_A$ receptors. **b**, The images display $GABA_A$ receptors in different 3D positions. The positional indications are best guesses performed by an experienced investigator. **c**, Overview images of otoferlin (right panel), and blank buffer as a control (left panel). **d**, Otoferlin images in different 3D positions. **e**, A FRC analysis of the resolution of such images indicates that the best resolution averages for $GABA_A$ receptors is 2.2 ± 0.03 nm (N = 5 analyses) and the best averages for otoferlin is 2.2 ± 0.007 nm (N = 5 analyses).

Supplementary Fig. 6. Calmodulin gallery. a, An overview of calmodulin ONE acquisitions in the presence and absence of calcium. This molecule was expressed and purified as a chimera containing mEGFP. The compact signal associated to the GFP molecule, as observed already in the TSR images in Fig. 1, has a limited contribution to the overall size of the molecule. **b**, Exemplary zoomed calmodulin ONE images. The asterisk denotes the best guess of GFP molecule bound to calmodulin.

Supplementary Fig. 7. A confocal analysis of synapses after MβCD treatments. a, Confocal images of hippocampal cultures immunostained for the three synaptic markers employed in Fig. 3a-c (Syt1, vGlut1 and PSD95), relying on the same staining protocol as in Fig. 3a-c. **b**, The panels show a magnified region. The culture morphology and synapse distribution are similar before and after MβCD treatments.

Supplementary Fig. 8. PSD95 model. a, To complement the distance analysis presented in Extended Data Fig. 7b, we analyzed the PSD95 distribution using a spot averaging procedure similar to a Ripley curve profile. To explain this analysis in more detail, we modeled it here. The top row of panels shows PSD-like spots, placed in a perfectly regular arrangement (left), with positions varying by 20 or 50% from perfect regularity (middle), or placed randomly (right). The bottom rows of panels show average spots, obtained by overlaying the areas surrounding each of the individual spots in the model arrangements from the top panels. This procedure results in arrangements in which the central spot is surrounded by increasingly weak spots, with virtually no regular spots around it in the right-most panel. **b**, Lines were drawn from the center of each spot in the bottom panels in panel a, in all directions, and were then averaged. The average line going from the center of a spot to the periphery shows a prominent peak if the arrangement is regular, since the neighboring spots are always present at a set distance, and thus provide a visible intensity peak. The less regular the arrangement is, the less clear the second peak becomes. It disappears completely when the spot positions are fully random.

Supplementary Fig. 9. The nanobody imaging of ASYN objects is specific and is not easily reproduced by antibodies. a, Low-resolution images of CSF-containing samples, or blanks (clean, BSA-coated coverslips). Only a few dim spots, presumably representing single nanobodies, are seen in the blanks. **b**, Quantification of the signal intensity, as a sum across all image pixels. N = 7-9; Mann-Whitney test, $P = 0.0002$. **c**, Individual examples of oligomers immunolabeled with nanobodies (top) or antibodies (bottom). **d**, Averages of ASYN objects from individual patients, immunolabeled with nanobodies or antibodies. **e**, An analysis of the average object size in antibody-labeled samples, as in Fig. 4. N = 2 patients for each condition; the graph shows mean ± range of values. Nanobodies reveal differences between patients, at object sizes of only a few nm. Antibodies have difficulties in this direction, as their large size causes a lower-fidelity labeling, and as their sizes obscure the actual sizes of small objects.

Supplementary Fig. 10. ONE analysis of SARS-CoV-2 viral particles. a, ONE overview of a sample containing SARS-CoV-2 viral particles immunostained against Spike Protein S1. **b**, More detailed views of two particles, indicating the Spike Protein S1 and the native IgG molecules from the serum of the patients. Interestingly, a domain-like structure is observed, which is presumably induced by the native IgGs gathering the spike proteins together, by the dual binding capacity of the IgG molecules.

Supplementary Tables

Supplementary Table 1. *Patient details.*

ID	Sex	Age	Diagnosis
1180	m	74	PD
1407	m	82	PD
1698	m	83	PD
1057	f	74	PD
1081	m	69	PD
1100	m	71	PD
1119	f	84	PD
861	f	60	RLS
906	m	73	CBD
1059	m	70	PSP
1223	f	77	PNP
1382	f	75	PNP
1529	m	84	PNP
1606	f	65	PNP

Average ages: 76.7 ± 2.3 years (PD), 72.0 ± 2.9 years (controls); no significant difference (Mann-Whitney Ranksum test).

PD: Parkinson's disease. CDB: Corticobasal degeneration. PNP: Peripheral neuropathy. PSP: Progressive supranuclear palsy. RLS: Restless legs syndrome.

Supplementary Table 2. *Image format and analysis technical information.*

Figure	Panel	Microscope	Objective	Number of frames	Resonant scanner frequency	Pixel size (nm)	Camera settings	SRRF analysis
1	a: ONE	TCS SP5 STED	100× 1.4 NA	1500-2000	8 kHz	0.98, 0.48	n.a.*	TRAC4
	a: ZOOM	Olympus TIRF	100× 1.49 NA	2000	n.a.	1	25 ms exposure, 300 EM Gain	TRAC4
	a: ExSTED	Abberior STED	100× 1.4 NA	n.a.	n.a.	2	n.a.	n.a.
	c	TCS SP5 STED	100× 1.4 NA	1500	8 kHz	0.98	n.a.	TRPPM, TRAC4
	d & f-g	TCS SP5 STED	100× 1.4 NA	1500	8 kHz	0.48	n.a.	TRAC4
2	a-d	TCS SP5 STED	100× 1.4 NA	1500	8 kHz	0.98	n.a.	TRPPM
	e	TCS SP5 STED	100× 1.4 NA	Up to 4000	8 kHz	0.98	n.a.	TRAC4
	g	TCS SP5 STED & TCS SP8 Lightning	100× 1.4 NA, 63× 1.41 NA	Up to 3000	8 kHz, 12 kHz, & 24, kHz	0.98, 0.48	n.a	TRAC4
	h	Leica TCS SP8 Lightning	63× 1.41 NA	Up to 400	24 kHz	0.98, 0.48	n.a	TRAC4
	i & k	TCS SP5 STED	TCS SP5 STED	2000	8 kHz	0.98	n.a.	TRPPM, TRAC4
3	a & b	Olympus TIRF	100× 1.49 NA	2000	n.a.	1	30 ms exposure, 300 EM Gain	TRPPM
	d	TCS SP5 STED	100× 1.4 NA	1500	8 kHz	0.98	n.a.	TRPPM, TRAC4
	e	Olympus TIRF	100× 1.49 NA	2000	n.a.	1	30 ms exposure, 300 EM Gain	TRPPM
	f	TCS SP5 STED	100× 1.4 NA	1500	8 kHz	0.98	n.a.	TRAC4
4	a & b	TCS SP5 STED	100× 1.4 NA	1500	8 kHz	0.98	n.a.	TRPPM, TRAC4
Extended data figure	**Panel**	**Microscope**	**Objective**	**Number of frames**	**Resonant scanner frequency**	**Pixel size (nm)**	**Camera settings**	**SRRF analysis**
1	b	TCS SP5 STED	100× 1.4 NA	1500	8 kHz	0.98	n.a.	TRAC4
2	c & f	TCS SP5 STED	100× 1.4 NA	Up to 4000	8 kHz	0.98	n.a.	TRAC4
4	a	TCS SP5 STED	100× 1.4 NA	1500	8 kHz	0.48	n.a.	TRAC4
	b & e	TCS SP5 STED	100× 1.4 NA	2000	8 kHz	0.4	n.a	TRAC4
5	b, d, & f	TCS SP5 STED	100× 1.4 NA	1500	8 kHz	0.98, 0.48	n.a.	TRAC4
6	a	Leica TCS SP8 Lightning	63× 1.41 NA	250	12 kHz & 24 kHz	0.96	n.a.	TRAC4
7	a	Leica TCS SP8 Lightning	63× 1.41 NA	250	12 kHz & 24 kHz	0.96	n.a.	TRAC4
8	a & b	Abberior STED	100× 1.4 NA	n.a.	n.a.	2	n.a.	n.a.

	c	Olympus TIRF	100× 1.49 NA	2000	n.a.	1	35 ms exposure, 300 EM Gain	TRPPM
9	c	TCS SP5 STED	100× 1.4 NA	1500	8 kHz	0.98	n.a.	TRAC4
10	-	TCS SP5 STED	100× 1.4 NA	1500	8 kHz	0.98	n.a.	TRAC4, TRPPM
Sup. figures	**Panel**	**Microscope**	**Objective**	**Number of frames**	**Resonant scanner frequency**	**Pixel size (nm)**	**Camera settings**	**SRRF analysis**
1	d	TCS SP5 STED	100× 1.4 NA	2000	8 kHz	0.98	n.a.	TRA, TRPPM, TRAC2 & 4
3	a & b	TCS SP5 STED	100× 1.4 NA	1500-2000	8 kHz	0.98, 0.48	n.a.	TRAC4
4	a, b, f, & h	TCS SP5 STED	100× 1.4 NA	Up to 2000	8 kHz	0.98	n.a.	TRPPM
5	A & b	TCS SP5 STED	100× 1.4 NA	Up to 5000	8 kHz	0.98	n.a.	TRAC4
	c & d	TCS SP5 STED	100× 1.4 NA	Up to 3000	8 kHz	0.98, 0.48	n.a.	TRAC4
6	a & b	TCS SP5 STED	100× 1.4 NA	Up to 2000	8 kHz	0.98	n.a.	TRPPM
9	c	TCS SP5 STED	100× 1.4 NA	1500	8 kHz	0.98	n.a.	TRAC4, TRPPM
10	a	Olympus TIRF	100× 1.49 NA	2000	n.a.	1	30 ms exposure, 300 EM Gain	TRPPM
	b	TCS SP5 STED	100× 1.4 NA	1500	8 kHz	0.98	n.a.	TRAC4

*n.a. not applicable.

Materials and Methods

Conventional cell cultures. Tubulin immunostaining was performed in the U2OS cell line, obtained from Cell Lines Service (CLS, Eppelheim, Germany). The cells were grown in a humidified incubator (5% CO_2, 37°C), in Dulbecco's Modified Eagle Medium (DMEM #D5671, Merck, Darmstadt, Germany), with the addition of 10% FCS (fetal calf serum, #S0615, Merck) and 4 mM glutamine (#25030-024, ThermoFisher Scientific, Waltham, USA), with an antibiotic mixture added at 1% (penicillin/streptomycin (ThermoFisher Scientific). For imaging purposes, cells were grown overnight on poly-L-lysine-coated coverslips (#P2658, Merck).

Hippocampal cultured neurons. Animals (Wistar rats, P0 to P1) were treated according to the regulations of the local authority, the Lower Saxony State Office for Consumer Protection and Food Safety (Niedersächsisches Landesamt für Verbraucherschutz und Lebensmittelsicherheit), under the license Tötungsversuch T09/08. In brief, the hippocampi were dissected from the brains, were washed with Hank's Balanced Salt Solution (HBSS, #14175-053, Invitrogen, Waltham, MA, USA), before being incubated under slow rotation in a digestion solution containing 15 U/ml papain (#LS003126, Worthington, Lakewood, USA), with 1 mM $CaCl_2$, 0.5 mM EDTA and 0.5 mg/ml L-cysteine (#30090, Merck), in DMEM. This procedure is performed for 1 hour at 37°C, before enzyme inactivation with a buffer containing 10% FCS and 5 mg/ml bovine serum albumin (BSA, #A1391, Applichem, Darmstadt, Germany) in DMEM. The inactivation solution is replaced after 15 minutes with the growth medium, containing 10% horse serum (#S900-500, VWR International GmbH, Darmstadt, Germany), 1.8 mM glutamine and 0.6 mg/ml glucose in MEM (#51200046, ThermoFisher Scientific), which is used to wash the hippocampi repeatedly. The neurons are then isolated by trituration using a glass pipette, and are sedimented by centrifugation at 800 rpm (8 minutes). The cells are then resuspended in the same medium and are seeded on PLL-coated coverslips, for several hours, before replacing the buffer with Neurobasal-

A culture medium (#10888-022, ThermoFisher Scientific), containing 0.2% B27-supplement (#17504-044; ThermoFisher Scientific) and 2 mM GlutaMAX (#35050-038, ThermoFisher Scientific). The neurons are then maintained in a humidified incubator (5% CO_2, 37°C) for at least 14 days before usage.

Brain slices. We dissected rat brains from P0-P1 rat pups (Wistar), as above. The brains were then fixed with 4% PFA (#30525894, Merck) in PBS, for 20 hours. The fixed brains were then placed in agarose (4% solution, #9012366, VWR Life Science, Hannover, Germany), before cutting to the desired thickness (100-200 µm) using a vibratome.

Patients. Patients were in treatment at Paracelsus Elena Klinik, Kassel, Germany. They had been diagnosed with Parkinson's disease according to standard criteria[70-72]. Neurological control patients had been diagnosed with a variety of non-neurodegenerative disorders. For a detailed presentation of patients, their ages and diagnoses, see Supplementary Table 1. The informed consent of all of the participants was obtained at the Paracelsus Elena Klinik, following the principles of the Declaration of Helsinki.

CSF samples. CSF samples were collected at the Paracelsus Elena Klinik, Kassel, Germany, following identical standard operating procedures (SOPs). CSF was gained by lumbar puncture in the morning with the patients fasting and in sitting position. The CSF was processed by centrifugation at 2000 x g for 10 minutes at room temperature and aliquots of supernatant frozen within 20-30 minutes and stored at -80 °C until analysis. Samples with red blood cell count>25/µl or indication for an inflammatory process were excluded.

Immunostaining procedures.

Tubulin immunostaining. U2OS cells were first incubated with 0.2% saponin (#47036, Sigma Aldrich), to extract lipid membranes. This procedure was performed for 1 minute in cytoskeleton buffer, consisting of 10 mM MES (#M3671, Merck), 138 mM KCl, 3 mM $MgCl_2$, 2 mM EGTA and 320 mM sucrose, at pH 6.1. The cells were then fixed, using 4% PFA and 0.1% Glutaraldehyde (#A3166, PanReac, Darmstadt, Germany), in the same buffer. Unreacted aldehyde groups were quenched using 0.1% NaBH4 (#71320, Sigma Aldrich now Merck), for 7 minutes in PBS, followed by a second quenching step with 0.1 M glycine (#3187, Carl Roth), for 10 minutes in PBS. The samples were blocked and simultaneously permeabilized using 2% BSA and 0.1% Triton X-100 (#9036-19-5, Sigma Aldrich), in PBS (room temperature, 30 minutes). Primary tubulin antibodies (#T6199 Sigma Aldrich, #302211 Synaptic Systems, Göttingen, Germany, #302203 Synaptic Systems, #ab18251 Abcam, Cambridge, UK) were first saturated with either secondary antibodies or secondary nanobodies (in separate experiments; #ST635P-1001, Abberior, Göttingen, Germany, and #N1202-Ab635P-S and #N2402-Ab635P-S, both NanoTag Biotechnologies GmbH, Göttingen, Germany) for 30 minutes at room temperature, using a ratio of 1:5 for the primary:secondary probes,

respectively. Afterwards, the antibody mixture was diluted in the blocking buffer, and was applied onto the cells for 60 minutes at room temperature. Five washes with permeabilization buffer followed by three PBS washes (each one for 10 minutes), before continuing with cellular expansion.

Neuronal immunostainings. Neurons were fixed with 4% PFA in PBS, for at least 30 minutes, before quenching with 50 mM glycine (in PBS) for 10 minutes, and blocking/permeabilizing using 2.5% BSA, 2.5% NGS, and 0.1% Triton X-100 in PBS (30 minutes at room temperature, unless specified elsewhere otherwise). The antibodies and/or primary nanobodies were diluted in 2.5% BSA, 2.5% NGS in PBS, and they were added to the coverslips for 60 minutes at room temperature. This was followed by washing with the permeabilization buffer (30 minutes, three buffer exchanges), and by the application of secondary antibodies or nanobodies, in the same buffer, for 45 minutes at room temperature. Specimens were then washed five times with permeabilization buffer and a final wash with PBS was then performed (15-30 minutes, three buffer exchanges). The primary antibodies used were anti synaptotagmin1 (SYT1, #105011 Synaptic Systems), anti Homer1 (#160 003, Synpatic Systems), anti Shank2 (#162204 Synaptic Systems), anti GluR2 (Alomone Labs, #AGC-005, Jerusalem, Israel), anti GluN2b (Neuromab 75-101, California, USA), anti MAP2 (Novus Biologicals #NB300-213), anti vGluT1 (#135304, Synaptic Systems), anti Bassoon (#ADI-VAM-PS003-F, Enzo, New York, USA). Primary nanobodies were FluoTag-X2 anti-PSD95 (clone 1B2, #N3702, NanoTag Biotechnologies GmbH). Secondary antibodies were conjugated to Alexa 405 (#ab175674, Abcam), Alexa Fluor 488 (AF488, #706-545-148, Dianova), Cy3 (#711-165-150, Jackson ImmunoResearch), Abberior STAR580 (AS580 #ST580-1006, Abberior), Abberior STAR635P (#2-0112-007-1, Abberior), FluoTag-X2 STAR635P #N2002-Ab635P and #N2402-Ab635P (NanoTag Biotechnologies GmbH).

Live immunostaining using synaptotagmin 1 antibodies. Surface Synaptotagmin 1 (Syt1) molecules were first blocked using unconjugated 604.2 Syt1 antibodies (#105311 Synaptic Systems), for 10 minutes at room temperature, in Tyrode buffer lacking Ca^{2+} (to reduce drastically both exo- and endocytosis; the Tyrode buffer contained 124 mM NaCl, 5 mM KCl, 2 mM $CaCl_2$, 1 mM $MgCl_2$, 30 mM glucose, 25 mM HEPES, at pH 7.4). The neurons were incubated over an ice water bath and exposed to fluorescently-conjugated Syt1 antibodies (#105311AT1, Synaptic Systems) for 40 minutes, to enable limited exo- and endocytosis. The neurons were then fixed with 4% PFA for 20 minutes, and quenched with 50 mM glycine for 10 minutes. The samples were then blocked with 2.5% BSA in PBS for 30 minutes and vGluT1 antibody was added prior to fixation and permeabilization for 1 h. Three brief washing steps with blocking buffer preceded the permeabilization step and neurons were labeled for PSD95 using the FluoTag-X2 anti-PSD95 nanobody (NanoTag Biotechnologies GmbH), as indicated above.

Immunostaining of cerebro-spinal fluid (CSF) samples. Cerebro-spinal fluid probes were obtained from PD patients and controls at the Paracelsus Elena Klinik (Kassel, Germany), and were stored at -80°C before use. 20 µl amounts of CSF were placed

on BSA-coated coverslips, enabling the sedimentation of multiprotein species overnight at 4° C. Fixation with 4% PFA (10 minutes, room temperature) and quenching with 50 mM glycine (10 minutes, room temperature) was followed by the application of either antibodies (Alpha-synuclein #128211 and 128002, Synaptic Systems) or Alpha-synuclein nanobody2[60], custom produced and fluorescently-conjugated by NanoTag) for 1 h at room temperature, in 2.5% BSA in PBS buffer. For the case of antibodies, secondary Aberrior STAR635P was applied for 1 h at room temperature. Five washes with 2.5% BSA in PBS were followed by mild post-fixation with 4% PFA for 4 min, and by the expansion procedures.

Brain slice immunostaining. The fixed brain slices were first quenched using 50 mM glycine (in PBS), followed by three washes with PBS (each for 5 minutes), and blocking and permeabilization in PBS containing 2.5% BSA and 0.3% Triton X-100, for 120 minutes at room temperature. The primary antibodies used (Bassoon, #ADI-VAM-PS003-F, Enzo Life Sciences GmbH, Lörrach, Germany; Homer1, #160003, Synaptic Systems) were diluted in the same buffer (lacking Triton X-100) to 2 µg/ml and were added to the slices overnight, at 4°C. Three washes with PBS (each for 5 minutes) removed the primary antibodies, enabling the addition of secondary antibodies conjugated with Abberior Star635P (#ST635P-1001, Abberior, Göttingen, Germany) for Basson identification, or with Cy3 (#711-165-152, Dianova, Hamburg, Germany) for Homer1 identification. The secondary antibodies were diluted to 1 µg/ml in PBS containing 2.5% BSA, and were incubated for 3 hours at room temperature. The brain slices were finally subjected to five washes with PBS containing 2.5% BSA (each wash for 5 minutes), followed by two final 5-minute washes in PBS.

Immunostaining of SARS-CoV-2 particles. Intact SARS-CoV-2 samples deposited by the Center for Disease Control and Prevention were obtained through BEI resources, NIAID, NIH: isolate USA-WA1/2020, NR-52281 (Cat# NATSARS(COV2)-ERC, ZeptoMetrix, USA). The samples consisted of patient serum containing viral particles, fixed chemically using aldehydes, in a buffer containing BSA. An average of 9200 viral particle were allowed to adsorb onto single BSA-coated coverslips overnight at 4° C. Samples were mildly fixed with 4% PFA for 4 min before immunostaining using anti SARS-CoV-2 Spike Protein S1 (Cat# PA5-114447, ThermoFIsher Scientific) and anti human IgG (Fc)-Alexa 488 (Cat# 109-545-170, Jackson ImmunoResearch), as described above.

GFP-nanobody complex (TSR) generation. The monomeric (A206K) and non-fluorescent (Y66L) EGFP (mEGFP*) was modified to have an ALFA-tag on the N-Terminus and a HaloTag on its C-terminus (ALFA-EGFP-HaloTag). This construct was expressed in a NebExpress bacterial strain, and it had an N-terminal HisTag, followed by a bdSUMO domain, which enables the specific cleavage of the HisTag[38] later on, after the purification procedures. Bacteria were grown at 37°C with shaking at 120 rpm in terrific broth (TB) supplemented with kanamycin. When reaching an optical density (OD) of ~3, the temperature was reduced to 30°C and bacteria were induced using 0.4 mM isopropyl β-D-1-thiogalactopyranoside (IPTG), with shaking for another ~16h. Bacteria lysates were incubated with Ni^{+} resin (Roche cOmplete) for 2h at 4°C. After

several washing steps, the ALFA-tag-mEGFP(Y66L)-HaloTag protein was eluted by enzymatic cleavage on the column by using 0.1 µM of SENP1 protease for 15 minutes. Protein concentration was determined using Nanodrop (ThermoFisher), and purity was assessed by Coomassie gels. Complex formation was performed by mixing, for 1h at room temperature, in a final volume of 40 µl, the following: 25 pmol of ALFA-EGFP-HaloTag and 30 pmol of 3 different single-domain antibodies: FluoTag-Q anti-ALFA (Cat# N1505), FluoTag-X2 anti-GFP (clone 1H1, Cat# N0301) and FluoTag-X2 anti-GFP (clone 1B2), all from NanoTag Biotechnologies GmbH. The control experiments were performed by a similar procedure, without including the target protein ALFA-EGFP-HaloTag.

Polyacrylamide gel electrophoresis (PAGE). A primary mouse monoclonal antibody against synaptobrevin 2 (Cat# 104 211, Synaptic Systems) and a secondary antibody conjugated to Abberrior Star635P (Cat#ST635P-1002-500UG) were mixed with reducing 2x Laemmli buffer (63 mM Tris-HCl pH 6.8, 2% SDS, 100 mM DTT, 20% glycerol) and heated for 10 minutes at 96°C. The denatured and reduced samples were then loaded in a self-cast Tris-glycine 12% polyacrylamide gel, and 10µg of total protein was loaded per lane. Electrophoresis was run at low voltage, at room temperature. The gel was briefly rinsed using distilled water and fluorescence was read on a GE-Healthcare AI-600 imager using a far-red filter (Cy5 channel). Next, the gel was submerged for 4 hours in Coomassie Brilliant Blue solution to stain all proteins, following by incubation with destaining solutions, before finally being imaged using the same GE-Healthcare AI 600 gel documentation system.

Dot Blot. In a stripe of nitrocellulose membrane (GE Healthcare), 5 mg of bovine serum albumin (BSA) and 1 µg of ALFA-tagged EGFP(Y66L)-HaloTag were spotted and let to dry at room temperature. Membranes were then blocked in PBS supplemented with 5% skim milk and 0.05% Tween-20 for 1 h with tilting/shaking. FluoTag X2 anti-GFP Cy3 (clone 1B1), FluoTag-X2 anti GFP-AberriorStar635P (clone 1H1) and Fluotag-X2 anti-ALFA AbberiorStar635P (all from NanoTag) were used at 2.5 nM final concentration in PBS with 5% milk and 0.05% Tween-20 for 1h with gentle rocking. After 1 h incubation at room temperature and protected from light, 5 washing steps using 2 ml each were performed with PBS supplemented with 0.05% Tween-20 for a total of 30 minutes. Membranes were finally imaged using a GE-Healthcare AI 600 system.

1,6-hexanediol treatments. This compound (#240117-50G, Aldrich) was diluted in the neuronal Neurobasal-A culture medium at 3% for 2 minutes, and 10% for 12 minutes, before fixation and further processing for immunostaining.

Purified proteins. Immunoglobulins A and M were purchased from Jackson ImmunoResearch and Immunoglobulinss G from Abberior, Göttingen, Germany (AffinityPure IgA, ChromePure IgM 009-000-012, and ST635P-1001, respectively) and were diluted in PBS, before expansion procedures. Otoferlin was produced according to standard procedures[73], and was diluted in 20 mM HEPES, 100 mM KCl, 0.05% DDM buffer, before being used at 0.4 mg/ml concentration. For $GABA_A$ receptors a construct

encoding the full-length human $GABA_A$ receptor b3 subunit (Uniprot ID P28472), with an N-terminus TwinStrep tag, was cloned into the pHR-CMV-TetO2 vector[74]. A lentiviral cell pool was generated in HEK293S GnTI-TetR cells as described previously[75]. Cells were grown in FreeStyle 293 expression medium (Gibco) supplemented with 1% fetal bovine serum (Gibco), 1mM L-Glutamine (Gibco), 1% NEEA (Gibco) and 5 mg/mL blasticidin (Invivogen) at 37 °C, 130 r.p.m., 8% CO2 and induced as described[76]. Following collection by centrifugation (2,000 g, 15 min), the cell pellets were resuspended in PBS, pH=8 supplemented with 1% (v/v) mammalian protease inhibitor cocktail (Sigma-Aldrich). Cell membranes were solubilized with 1% (w/v) n-dodecyl β-D-maltopyranoside (DDM, Anatrace) for 1h. The insoluble material was removed by centrifugation (12,500g, 15 min) and the supernatant was incubated with 300 mL Strep-Tactin® Superflow® resin (IBA lifesciences) while rotating slowly for 2h at 4°C. The beads were collected by centrifugation (300g, 5 min) and washed with 150mL of 0.04% (w/v) DDM, PBS pH=8. The sample was eluted in 2.5 mM Biotin, 0.02% (w/v) DDM, PBS pH=8 and used for imaging at 1 mg/mL concentration. Calmodulin was purified as previously described[77], and was used in calcium free buffer: 150 mM KCl, 10 mM HEPES, 5 mM EGTA, or calcium+ buffer: 150 mM KCL, 10 mM HEPES, 2 mM $CaCl_2$, at pH = 7.2, before expansion procedures. In brief, calmodulin 1 (mRNA reference sequence number NM_031969.2) was tagged with mEGFP and an ALFA-tag, for affinity purification purposes. The construct was transfected in HEK293 cells using Lipofectamine 2000 (Invitrogen, Carlsbad, CA, USA), following the manufacturer's protocol. After expression for ~24 hours, the cells were lysed in a PBS buffer containing 1% Triton X-100, 2 mM EDTA and a protease inhibitor cocktail. The debris was removed by centrifugation, and the supernatant was added to an ALFA Selector PE resin (NanoTag Biotechnologies), where it was allowed to bind for 60 minutes (4°C, under rotation). After two washes with lysis buffer and one wash with PBS (ice-cold), the bound proteins were eluted by adding the ALFA peptide. The purified protein was analyzed by Coomassie gel imaging (published in[77]).

Expansion procedures. X10 expansion of cultured cells was performed using proteinase K exactly as described in the following protocol article:[28]. X10 expansion relying on autoclaving (X10ht[69]) was performed as follows. The samples were incubated with 0.3 mg/ml Acryloyl-X (SE; #A-20770, Thermo Fisher Scientific) in alkaline buffer (150 mN $NaHCO_3$, pH 6.4), overnight, at room temperature. The samples were then subjected to three PBS washes (5 minutes each), while preparing the gel monomer solution, exactly as described[28]. The solution was pipetted on parafilm and was covered by upside-down coverslips containing cells, or with brain slices that were then also covered with fresh coverslips. Polymerization was allowed to proceed overnight at room temperature, in a humidified chamber. Homogenization of proteins and single molecules were performed using 8 U/ml proteinase K (PK, #P4850 Sigma Aldrich now Merck) in digestion buffer (800 mM guanidine HCl, 2 mM $CaCl_2$, 0.5 % Triton X-100, in 50 mM TRIS), overnight at 50°C. Homogenization of cell cultures and brain slices was done by autoclaving for 60 minutes at 110°C in disruption buffer (5% Triton-X and 1% SDS in 100 mM TRIS, pH 8.0) followed by a 90 minutes incubation for temperature to cool down to safe levels. Before autoclaving, the gels

were first washed using 1 M NaCl, and were then washed at least four times in disruption buffer, for a total time of at least 120 minutes. Gel expansion was then performed by ddH_2O washing, for several hours, with at least five solution exchanges. Expansion was performed in 22 x 22 cm square culture dishes, carrying 400-500 ml ddH_2O. When desired, the samples were labeled using 20-fold molar excess of NHS-ester fluorescein (#46409, ThermoFisher Scientific) in $NaCHO_3$ buffer at pH = 8.3 for 1 h, before the washing procedure that induced the final expansion.

ZOOM expansion procedures. Fixed U2OS cultured cells were incubated in anchoring solution (25 mM Acrylic acid N-hydroxysuccinimide ester in 60% v/v DPBS and 40% v/v DMSO) for 60 minutes. Afterward, cells were moved to monomer solution (30% w/v Acrylamide and 0.014% w/v N-N'-methylenbisacrylamide in PBS buffer). After 60 min, the gelation process was started by adding initiators (0.5% w/v TEMED and 0.5% w/v APS) to the monomer solution. The hydrogel-cell hybrid was homogenized in detergent solution (200 mM SDS, 50 mM boric acid in DI water, pH titrated to 9.0), at 95 °C for 15 min, following by 24 h at 80 °C. ZOOM-processed samples were then stained using the previously mentioned anti α-tubulin antibodies (1:400 in PBST).

Microscope systems. For image acquisition, small gel fragments were cut and were placed in the imaging chamber presented in Supplementary Fig. 2. Paper tissues were used to remove any water droplets around the gels, before enabling the gels to equilibrate for at least 30 minutes on the microscope stage. Epifluorescence imaging was performed using an Olympus IX83 TIRF microscope equipped with an Andor iXon Ultra 888, 100× 1.49 NA TIRF objective, and an Olympus LAS-VC 4-channel laser illumination system. Confocal imaging was performed, for most experiments, using a TCS SP5 STED microscope (Leica Microsystems, Wetzlar, Germany), using a HCX Plan Apochromat STED objective, 100×, 1.4 NA, oil immersion. The LAS AF imaging software (Leica) was used to operate imaging experiments. Excitation lines were 633, 561, and 488 nm, and emission was tuned using an acousto-optical tunable filter. Detection was ensured by PMT and HyD detectors. Images were taken using a resonant scanner at 8 kHz frequency. 5D-stacks for zONE were performed using a 12 kHz resonant scanner mounted on a Leica TCSSP8 Lightning confocal microscope. Samples were excited with a 40% white light laser (WLL) at wavelengths of 633, 561 and 488 nm, and acquisitions were carried out using HyD detectors in unidirectional-xyct line scans or in uni- and bi-directional xyczt line scans.

Image acquisition. Objectives of 1.4, 1.45 and 1.51 NA were used to acquire images with a theoretical pixel size of 98 nm. For a higher resolution, the theoretical pixel size was set to 48 nm, at the cost of slightly lower detection rate. Images acquired on camera-based system had a predetermined pixel size of 100 nm. The acquisition speeds were ranging between 20 to 40 ms and 25 ms on a resonant scanner of 8 kHz and on a camera, respectively, for xyct. For hyperstacks of xyczt acquisitions, images were acquired using 8 kHz and 12 kHz scanners in bidirectional mode (after the necessary alignments) to compensate for speed loss. Images of 8 bit depth were acquired at a line format ranging from 128x128 to 256x256. The scanning modality on a confocal was set to "minimize time interval" (Leica LAS software). To maintain natural

fluctuations of fluorophores, we did not use line accumulation or line averaging during scanning. A frame count starting from 200 and up to 4000 were acquired. We recommend a frame count of at least 1500 to 2000 for optimal computed resolution.

Image processing. ONE image processing is enabled through a Java-written ONE Platform under “ONE microscopy” in Fiji. The ONE microscopy plugin utilizes open-source codes from Bioformats Java library, NanoJ-Core, NanoJ-SRRF, NanoJ-eSRRF, and Image Stabilizer[6,7,78,79]. ONE plugin supports multiple video formats of single or batch analyses in xyct. Hyperstacks with 5-dimensions xyczt format are processed with zONE module. This module allows the user to select the optical slices and channels to resolve at ultra-resolution. Upon irregularities in resolving 1 or more channels within 1 or more planes, zONE leaves a blank image, and computes the remaining planes within a stack. The image processing is fully automated and requires minimal initial user input. Aside from the expansion factor, preset values and analysis modalities are automatically provided (for more details, see Supplementary Fig. 1). The ONE plugin has a pre-installed safety protocol to skip failures in computations or uncompensated drifts, without affecting the progress of batch analysis. Data analysis, parameters and irregularities are reported in log files. The ONE plugin automatically linearizes the scale, based on radiality magnification and expansion factor corrections. In addition, ONE offers the possibility to correct for chromatic aberration by processing multi-channel bead images as a template that is applied to super-resolved images of the biological samples. The correction is performed by applying the Lucas-Kanade algorithm[78]. For the ONE Microscopy plugin to store complex multi-dimension images from hyperstacks, we modified the Java code of the ImageJ library and adapted it locally. ONE Platform source code and plugin are available on https://www.rizzoli-lab.de/ONE. For best performance, we recommend to download a preinstalled version on Fiji available via the same link.

Image analysis and statistics. For single-object analyses, such as synaptic vesicle or antibody analyses, signal intensities and distances between objects were analyzed manually using ImageJ (Wayne Rasband and contributors, National Institutes of Health, USA). Line scans were also performed and analyzed using ImageJ. For the analysis of PSDs (Fig. 2), spots were identified by thresholding band-pass filtered images, relying on empiric thresholds and band-pass filters, organized in the form of semi-automated routines in Matlab (version 2017b, The Mathworks, Inc, Natick, MA, USA). Spots were either overlaid, to determine their overall signal distributions, or their center positions were determined, to measure distances between spots (in either the same or different channels). The same procedure was used for the averaging analysis of CSF samples (Fig. 4) and for the analysis of spot distances for the GFP-nanobody assemblies (Extended Data Fig. 5). FWHM values were measured after performing line scans over small but distinguishable spots, as indicated in Fig. 1, followed by Gaussian fitting, using Matlab. Plots and statistics were generated using GraphPad Prism 9.3.1 (GraphPad Software Inc., La Jolla, CA, USA) or SigmaPlot 10 (Systat Software Inc., San Jose, CA, USA), or using Matlab. Statistics details are presented in

the respective figures. Figures were prepared with CorelDraw 23.5 (Corel Corporation, Ottawa, Ontario, Canada).

Ethics statement

Animals (Wistar rats, P0 to P1) were treated according to the regulations of the local authority, the Lower Saxony State Office for Consumer Protection and Food Safety (Niedersächsisches Landesamt für Verbraucherschutz und Lebensmittelsicherheit), under the license Tötungsversuch T09/08. For human patients, the informed consent of all of the participants was obtained at the Paracelsus Elena Klinik, following the principles of the Declaration of Helsinki.

Acknowledgements

We thank Christina Zeising and Jannik Hentze for excellent technical assistance. We thank Ali Kassem (Beirut, Lebanon) for driver debugging and integration. We thank Nils Brose (Max Planck Institute for Multidisciplinary Sciences, Göttingen, Germany) for help with access to his fluorescence microscopy facility. We thank Markus Krone (Max Planck Institute for Multidisciplinary Sciences, Göttingen, Germany) for support in building the gel stabilization chambers. We thank Eugenio Fornasiero and Christian Tetzlaff (University Medical Center Göttingen, Germany) and G.B. Rizzoli for comments on the initial manuscript. The work was supported by grants from the German Ministry for Education and Research, 13N15328/NG-FLIM and from the German Research Foundation (Deutsche Forschungsgemeinschaft, DFG), SFB1286/A03/B02/Z04, SFB1190/P09, and RI 1967/10-1 (NeuroNex) to S.O.R., the European Research Council (ERC) under the European Union's Horizon 2020 research and innovation programme (grant agreements No 835102 and 964016), and the DFG under Germany's Excellence Strategy - EXC 2067/1- 390729940. Support from the DFG grant SFB894/A9 (to UB) and the UK Medical Research Council grants MR/L009609/1 and MC_UP_1201/15 (to A.R.A.) is also acknowledged.

Data availability statement

Image data are available from the corresponding authors on reasonable request.

Author contributions

AHS and SOR conceived the project. AAC and UB developed the ONE Platform plugin. AHS and SOR designed and performed the experiments. AHS, VI and SOR analyzed the data. RC, NM and PF contributed to the tubulin experiments. SVG contributed to

the 1,6-hexanediol experiments. MM and JP purified otoferlin protein. HC and TM generated the otoferlin AlphaFold model. DM and ARA generated the $GABA_A$ receptors. SR purified calmodulin protein. FO generated the TSRs. DC generated the tissue sections. KAS assisted with the initial implementation of X10ht experiments. CT and BM provided the patient CSF specimens. TFO verified the analysis of the PD data. MS contributed to the understanding of photophysics fluctuations and ESB contributed to the understanding of ExM gel behavior. SOR wrote the manuscript, which was revised by all other authors, with especially strong contributions from AHS, ARA, MS and ESB.

Competing interests

S.O.R. and F.O. are shareholders of NanoTag Biotechnologies GmbH. The remaining authors declare no competing interests. E.S.B. is an inventor on multiple patents related to expansion microscopy, and co-founder of a company working on commercial applications of expansion microscopy.

References

1 Renz, M. Fluorescence microscopy-a historical and technical perspective. *Cytometry A* **83**, 767-779 (2013). https://doi.org:10.1002/cyto.a.22295

2 Bond, C., Santiago-Ruiz, A. N., Tang, Q. & Lakadamyali, M. Technological advances in super-resolution microscopy to study cellular processes. *Mol Cell* **82**, 315-332 (2022). https://doi.org:10.1016/j.molcel.2021.12.022

3 Liu, S., Hoess, P. & Ries, J. Super-Resolution Microscopy for Structural Cell Biology. *Annu Rev Biophys* **51**, 301-326 (2022). https://doi.org:10.1146/annurev-biophys-102521-112912

4 Schermelleh, L. *et al.* Super-resolution microscopy demystified. *Nat Cell Biol* **21**, 72-84 (2019). https://doi.org:10.1038/s41556-018-0251-8

5 Sigal, Y. M., Zhou, R. & Zhuang, X. Visualizing and discovering cellular structures with super-resolution microscopy. *Science* **361**, 880-887 (2018). https://doi.org:10.1126/science.aau1044

6 Gustafsson, N. *et al.* Fast live-cell conventional fluorophore nanoscopy with ImageJ through super-resolution radial fluctuations. *Nat Commun* **7**, 12471 (2016). https://doi.org:10.1038/ncomms12471

7 Laine, R. F. *et al.* High-fidelity 3D live-cell nanoscopy through data-driven enhanced super-resolution radial fluctuation. *bioRxiv*, 2022.2004.2007.487490 (2022). https://doi.org:10.1101/2022.04.07.487490

8 Balzarotti, F. *et al.* Nanometer resolution imaging and tracking of fluorescent molecules with minimal photon fluxes. *Science* **355**, 606-612 (2017). https://doi.org:10.1126/science.aak9913

9 Bates, M. *et al.* Optimal precision and accuracy in 4Pi-STORM using dynamic spline PSF models. *Nat Methods* **19**, 603-612 (2022). https://doi.org:10.1038/s41592-022-01465-8

10 Luciano A. Masullo, A. M. S., Lucía F. Lopez, Mauricio Pilo-Pais, Guillermo P. Acuna & Fernando D. Stefani. An alternative to MINFLUX that enables nanometer resolution in a confocal microscope. *Light: Science & Applications* (2022).

11 Weber, M. *et al.* MINSTED nanoscopy enters the Ångström localization range. *bioRxiv*, 2022.2003.2018.484906 (2022). https://doi.org:10.1101/2022.03.18.484906

12 Lelek, M. *et al.* Single-molecule localization microscopy. *Nat Rev Methods Primers* **1** (2021). https://doi.org:10.1038/s43586-021-00038-x

13 Helmerich, D. A. *et al.* Sub-10 nm fluorescence imaging. *bioRxiv*, 2022.2002.2008.479592 (2022). https://doi.org:10.1101/2022.02.08.479592

14 Chen, F., Tillberg, P. W. & Boyden, E. S. Optical imaging. Expansion microscopy. *Science* **347**, 543-548 (2015). https://doi.org:10.1126/science.1260088

15 Cahoon, C. K. *et al.* Superresolution expansion microscopy reveals the three-dimensional organization of the Drosophila synaptonemal complex. *Proc Natl Acad Sci U S A* **114**, E6857-E6866 (2017). https://doi.org:10.1073/pnas.1705623114

16 Gambarotto, D. *et al.* Imaging cellular ultrastructures using expansion microscopy (U-ExM). *Nat Methods* **16**, 71-74 (2019). https://doi.org:10.1038/s41592-018-0238-1
17 Gao, M. *et al.* Expansion Stimulated Emission Depletion Microscopy (ExSTED). *ACS Nano* **12**, 4178-4185 (2018). https://doi.org:10.1021/acsnano.8b00776
18 Halpern, A. R., Alas, G. C. M., Chozinski, T. J., Paredez, A. R. & Vaughan, J. C. Hybrid Structured Illumination Expansion Microscopy Reveals Microbial Cytoskeleton Organization. *ACS Nano* **11**, 12677-12686 (2017). https://doi.org:10.1021/acsnano.7b07200
19 Kim, D., Kim, T., Lee, J. & Shim, S. H. Amplified Expansion Stimulated Emission Depletion Microscopy. *Chembiochem* **20**, 1260-1265 (2019). https://doi.org:10.1002/cbic.201800775
20 Li, R., Chen, X., Lin, Z., Wang, Y. & Sun, Y. Expansion enhanced nanoscopy. *Nanoscale* **10**, 17552-17556 (2018). https://doi.org:10.1039/c8nr04267e
21 Wang, Y. *et al.* Combined expansion microscopy with structured illumination microscopy for analyzing protein complexes. *Nat Protoc* **13**, 1869-1895 (2018). https://doi.org:10.1038/s41596-018-0023-8
22 Xu, H. *et al.* Molecular organization of mammalian meiotic chromosome axis revealed by expansion STORM microscopy. *Proc Natl Acad Sci U S A* **116**, 18423-18428 (2019). https://doi.org:10.1073/pnas.1902440116
23 Hell, S. W. & Wichmann, J. Breaking the diffraction resolution limit by stimulated emission: stimulated-emission-depletion fluorescence microscopy. *Opt Lett* **19**, 780-782 (1994). https://doi.org:10.1364/ol.19.000780
24 Gustafsson, M. G. Nonlinear structured-illumination microscopy: wide-field fluorescence imaging with theoretically unlimited resolution. *Proc Natl Acad Sci U S A* **102**, 13081-13086 (2005). https://doi.org:10.1073/pnas.0406877102
25 Betzig, E. *et al.* Imaging intracellular fluorescent proteins at nanometer resolution. *Science* **313**, 1642-1645 (2006). https://doi.org:10.1126/science.1127344
26 Dertinger, T., Colyer, R., Iyer, G., Weiss, S. & Enderlein, J. Fast, background-free, 3D super-resolution optical fluctuation imaging (SOFI). *Proc Natl Acad Sci U S A* **106**, 22287-22292 (2009). https://doi.org:10.1073/pnas.0907866106
27 Truckenbrodt, S. *et al.* X10 expansion microscopy enables 25-nm resolution on conventional microscopes. *EMBO Rep* **19** (2018). https://doi.org:10.15252/embr.201845836
28 Truckenbrodt, S., Sommer, C., Rizzoli, S. O. & Danzl, J. G. A practical guide to optimization in X10 expansion microscopy. *Nat Protoc* **14**, 832-863 (2019). https://doi.org:10.1038/s41596-018-0117-3
29 Culley, S., Tosheva, K. L., Matos Pereira, P. & Henriques, R. SRRF: Universal live-cell super-resolution microscopy. *Int J Biochem Cell Biol* **101**, 74-79 (2018). https://doi.org:10.1016/j.biocel.2018.05.014
30 Bani H. Cipriano, T. K., Xin Zhang, and Srinivasa R. Raghavan. A Simple Method To Improve the Clarity and Rheological Properties of Polymer/Clay Nanocomposites by Using Fractionated Clay Particles. *ACS Applied Materials & Interfaces*, 130-135 (2009).
31 Gao, R. *et al.* A highly homogeneous polymer composed of tetrahedron-like monomers for high-isotropy expansion microscopy. *Nat Nanotechnol* **16**, 698-707 (2021). https://doi.org:10.1038/s41565-021-00875-7
32 Park, H. E. *et al.* Scalable and Isotropic Expansion of Tissues with Simply Tunable Expansion Ratio. *Adv Sci (Weinh)* **6**, 1901673 (2019). https://doi.org:10.1002/advs.201901673
33 Culley, S. *et al.* Quantitative mapping and minimization of super-resolution optical imaging artifacts. *Nat Methods* **15**, 263-266 (2018). https://doi.org:10.1038/nmeth.4605
34 Almada, P. *et al.* Automating multimodal microscopy with NanoJ-Fluidics. *Nat Commun* **10**, 1223 (2019). https://doi.org:10.1038/s41467-019-09231-9
35 Mikhaylova, M. *et al.* Resolving bundled microtubules using anti-tubulin nanobodies. *Nat Commun* **6**, 7933 (2015). https://doi.org:10.1038/ncomms8933
36 Weber, K., Rathke, P. C. & Osborn, M. Cytoplasmic microtubular images in glutaraldehyde-fixed tissue culture cells by electron microscopy and by immunofluorescence microscopy. *Proc Natl Acad Sci U S A* **75**, 1820-1824 (1978). https://doi.org:10.1073/pnas.75.4.1820
37 Sograte-Idrissi, S. *et al.* Nanobody Detection of Standard Fluorescent Proteins Enables Multi-Target DNA-PAINT with High Resolution and Minimal Displacement Errors. *Cells* **8** (2019). https://doi.org:10.3390/cells8010048
38 Gotzke, H. *et al.* The ALFA-tag is a highly versatile tool for nanobody-based bioscience applications. *Nat Commun* **10**, 4403 (2019). https://doi.org:10.1038/s41467-019-12301-7
39 Damstra, H. G. J. *et al.* Visualizing cellular and tissue ultrastructure using Ten-fold Robust Expansion Microscopy (TREx). *Elife* **11** (2022). https://doi.org:10.7554/eLife.73775
40 M'Saad, O. & Bewersdorf, J. Light microscopy of proteins in their ultrastructural context. *Nat Commun* **11**, 3850 (2020). https://doi.org:10.1038/s41467-020-17523-8

41 Miller, P. S. & Aricescu, A. R. Crystal structure of a human GABAA receptor. *Nature* **512**, 270-275 (2014). https://doi.org:10.1038/nature13293
42 Sente, A. *et al.* Differential assembly diversifies GABAA receptor structures and signalling. *Nature* **604**, 190-194 (2022). https://doi.org:10.1038/s41586-022-04517-3
43 Roux, I. *et al.* Otoferlin, defective in a human deafness form, is essential for exocytosis at the auditory ribbon synapse. *Cell* **127**, 277-289 (2006). https://doi.org:10.1016/j.cell.2006.08.040
44 Jumper, J. *et al.* Highly accurate protein structure prediction with AlphaFold. *Nature* **596**, 583-589 (2021). https://doi.org:10.1038/s41586-021-03819-2
45 Gan, Q. & Watanabe, S. Synaptic Vesicle Endocytosis in Different Model Systems. *Front Cell Neurosci* **12**, 171 (2018). https://doi.org:10.3389/fncel.2018.00171
46 Wienisch, M. & Klingauf, J. Vesicular proteins exocytosed and subsequently retrieved by compensatory endocytosis are nonidentical. *Nat Neurosci* **9**, 1019-1027 (2006). https://doi.org:10.1038/nn1739
47 Mutch, S. A. *et al.* Protein quantification at the single vesicle level reveals that a subset of synaptic vesicle proteins are trafficked with high precision. *J Neurosci* **31**, 1461-1470 (2011). https://doi.org:10.1523/JNEUROSCI.3805-10.2011
48 Takamori, S. *et al.* Molecular anatomy of a trafficking organelle. *Cell* **127**, 831-846 (2006). https://doi.org:10.1016/j.cell.2006.10.030
49 Dani, A., Huang, B., Bergan, J., Dulac, C. & Zhuang, X. Superresolution imaging of chemical synapses in the brain. *Neuron* **68**, 843-856 (2010). https://doi.org:10.1016/j.neuron.2010.11.021
50 Helm, M. S. *et al.* A large-scale nanoscopy and biochemistry analysis of postsynaptic dendritic spines. *Nat Neurosci* **24**, 1151-1162 (2021). https://doi.org:10.1038/s41593-021-00874-w
51 Hayashi, Y., Ford, L. K., Fioriti, L., McGurk, L. & Zhang, M. Liquid-Liquid Phase Separation in Physiology and Pathophysiology of the Nervous System. *J Neurosci* **41**, 834-844 (2021). https://doi.org:10.1523/JNEUROSCI.1656-20.2020
52 Alberti, S., Gladfelter, A. & Mittag, T. Considerations and Challenges in Studying Liquid-Liquid Phase Separation and Biomolecular Condensates. *Cell* **176**, 419-434 (2019). https://doi.org:10.1016/j.cell.2018.12.035
53 Rich, A. *The illustrated companion to the Latin dictionary, and Greek lexicon*. 552 (Longman, 1849).
54 Biederer, T., Kaeser, P. S. & Blanpied, T. A. Transcellular Nanoalignment of Synaptic Function. *Neuron* **96**, 680-696 (2017). https://doi.org:10.1016/j.neuron.2017.10.006
55 Spillantini, M. G. *et al.* Alpha-synuclein in Lewy bodies. *Nature* **388**, 839-840 (1997). https://doi.org:10.1038/42166
56 Uversky, V. N. A protein-chameleon: conformational plasticity of alpha-synuclein, a disordered protein involved in neurodegenerative disorders. *J Biomol Struct Dyn* **21**, 211-234 (2003). https://doi.org:10.1080/07391102.2003.10506918
57 Bruggink, K. A., Kuiperij, H. B., Ekholm-Pettersson, F. & Verbeek, M. M. Detection of elevated levels of alpha-synuclein oligomers in CSF from patients with Parkinson disease. *Neurology* **77**, 510; author reply 510-511 (2011). https://doi.org:10.1212/WNL.0b013e318219dd92
58 Mollenhauer, B. *et al.* Direct quantification of CSF alpha-synuclein by ELISA and first cross-sectional study in patients with neurodegeneration. *Exp Neurol* **213**, 315-325 (2008). https://doi.org:10.1016/j.expneurol.2008.06.004
59 Tokuda, T. *et al.* Decreased alpha-synuclein in cerebrospinal fluid of aged individuals and subjects with Parkinson's disease. *Biochem Biophys Res Commun* **349**, 162-166 (2006). https://doi.org:10.1016/j.bbrc.2006.08.024
60 De Genst, E. J. *et al.* Structure and properties of a complex of alpha-synuclein and a single-domain camelid antibody. *J Mol Biol* **402**, 326-343 (2010). https://doi.org:10.1016/j.jmb.2010.07.001
61 Guerrero-Ferreira, R. *et al.* Two new polymorphic structures of human full-length alpha-synuclein fibrils solved by cryo-electron microscopy. *Elife* **8** (2019). https://doi.org:10.7554/eLife.48907
62 Li, B. *et al.* Cryo-EM of full-length alpha-synuclein reveals fibril polymorphs with a common structural kernel. *Nat Commun* **9**, 3609 (2018). https://doi.org:10.1038/s41467-018-05971-2
63 Winner, B. *et al.* In vivo demonstration that alpha-synuclein oligomers are toxic. *Proc Natl Acad Sci U S A* **108**, 4194-4199 (2011). https://doi.org:10.1073/pnas.1100976108
64 Zhang, H., Griggs, A., Rochet, J. C. & Stanciu, L. A. In vitro study of alpha-synuclein protofibrils by cryo-EM suggests a Cu(2+)-dependent aggregation pathway. *Biophys J* **104**, 2706-2713 (2013). https://doi.org:10.1016/j.bpj.2013.04.050
65 Wassie, A. T., Zhao, Y. & Boyden, E. S. Expansion microscopy: principles and uses in biological research. *Nat Methods* **16**, 33-41 (2019). https://doi.org:10.1038/s41592-018-0219-4

66 Chen, B. C. *et al.* Lattice light-sheet microscopy: imaging molecules to embryos at high spatiotemporal resolution. *Science* **346**, 1257998 (2014). https://doi.org:10.1126/science.1257998

67 Eilers, Y., Ta, H., Gwosch, K. C., Balzarotti, F. & Hell, S. W. MINFLUX monitors rapid molecular jumps with superior spatiotemporal resolution. *Proc Natl Acad Sci U S A* **115**, 6117-6122 (2018). https://doi.org:10.1073/pnas.1801672115

68 Gwosch, K. C. *et al.* MINFLUX nanoscopy delivers 3D multicolor nanometer resolution in cells. *Nat Methods* **17**, 217-224 (2020). https://doi.org:10.1038/s41592-019-0688-0

69 Saal, K.-A. *et al.* Heat denaturation enables multicolor X10-STED microscopy at single-digit nanometer resolution. *bioRxiv*, 2022.2006.2024.497479 (2022). https://doi.org:10.1101/2022.06.24.497479

70 Dubois, B. *et al.* Research criteria for the diagnosis of Alzheimer's disease: revising the NINCDS-ADRDA criteria. *Lancet Neurol* **6**, 734-746 (2007). https://doi.org:10.1016/S1474-4422(07)70178-3

71 Gibb, W. R. Accuracy in the clinical diagnosis of parkinsonian syndromes. *Postgrad Med J* **64**, 345-351 (1988). https://doi.org:10.1136/pgmj.64.751.345

72 McKeith, I. *et al.* Dementia with Lewy bodies. *Lancet Neurol* **3**, 19-28 (2004). https://doi.org:10.1016/s1474-4422(03)00619-7

73 Pullara, F. *et al.* A general path for large-scale solubilization of cellular proteins: from membrane receptors to multiprotein complexes. *Protein Expr Purif* **87**, 111-119 (2013). https://doi.org:10.1016/j.pep.2012.10.007

74 Aricescu, A. R., Lu, W. & Jones, E. Y. A time- and cost-efficient system for high-level protein production in mammalian cells. *Acta Crystallogr D Biol Crystallogr* **62**, 1243-1250 (2006). https://doi.org:10.1107/S0907444906029799

75 Elegheert, J. *et al.* Lentiviral transduction of mammalian cells for fast, scalable and high-level production of soluble and membrane proteins. *Nat Protoc* **13**, 2991-3017 (2018). https://doi.org:10.1038/s41596-018-0075-9

76 Masiulis, S. *et al.* GABAA receptor signalling mechanisms revealed by structural pharmacology. *Nature* **565**, 454-459 (2019). https://doi.org:10.1038/s41586-018-0832-5

77 Perego, E. *et al.* A minimalist model to measure interactions between proteins and synaptic vesicles. *Sci Rep* **10**, 21086 (2020). https://doi.org:10.1038/s41598-020-77887-1

78 Li, K. *The image stabilizer plugin for ImageJ*, 2008).

79 Linkert, M. *et al.* Metadata matters: access to image data in the real world. *J Cell Biol* **189**, 777-782 (2010). https://doi.org:10.1083/jcb.201004104

Extended Data Figures

Expansion microscopy at one nanometer resolution

Ali H. Shaib[1,*], Abed Alrahman Chouaib[2], Vanessa Imani[1], Rajdeep Chowdhury[1], Svilen Veselinov Georgiev[1], Nikolaos Mougios[1,3], Mehar Monga[4], Sofiia Reshetniak[1], Daniel Mihaylov[5], Han Chen[6], Parisa Fatehbasharzad[1], Dagmar Crzan[1], Kim-Ann Saal[1], Claudia Trenkwalder[7,8], Brit Mollenhauer[8,9], Tiago F. Outeiro[10], Julia Preobraschenski[4,11], Ute Becherer[2], Tobias Moser[6,11,12], Edward S. Boyden[13], A Radu Aricescu[5], Markus Sauer[14], Felipe Opazo[1,3,15], Silvio O. Rizzoli[1,3,11,*]

[1] Institute for Neuro- and Sensory Physiology, University Medical Center Göttingen, Göttingen, Germany

[2] Department of Cellular Neurophysiology, Center for Integrative Physiology and Molecular Medicine (CIPMM), Saarland University, Homburg, Germany

[3] Center for Biostructural Imaging of Neurodegeneration, University Medical Center Göttingen, Göttingen, Germany

[4] Biochemistry of Membrane Dynamics Group, Institute for Auditory Neuroscience, University Medical Center Göttingen, Göttingen, Germany

[5] MRC Laboratory of Molecular Biology, Cambridge, UK.

[6] Institute for Auditory Neuroscience and InnerEarLab, University Medical Center Göttingen, Göttingen, Germany

[7] Department of Neurosurgery, University Medical Center, Göttingen, Germany

[8] Paracelsus-Elena-Klinik, Kassel, Germany

[9] Department of Neurology, University Medical Center, Göttingen, Germany

[10] Department of Experimental Neurodegeneration, Center for Biostructural Imaging of Neurodegeneration, University Medical Center Göttingen, 37073 Göttingen, Germany; Max Planck Institute for Multidisciplinary Sciences, 37075 Göttingen, Germany; Translational and Clinical Research Institute, Faculty of Medical Sciences, Newcastle University, NE2 4HH, United Kingdom; Scientific Employee with an Honorary Contract at German Center for Neurodegenerative Diseases (DZNE), 37075 Göttingen, Germany

[11] Cluster of Excellence "Multiscale Bioimaging: from Molecular Machines to Networks of Excitable Cells" (MBExC), University of Goettingen, Göttingen, Germany

[12] Auditory Neuroscience and Synaptic Nanophysiology Group, Max Planck Institute for Multidisciplinary Sciences, Göttingen, Germany

[13] Department of Brain and Cognitive Sciences, Massachusetts Institute of Technology, Cambridge, MA, USA; Department of Biological Engineering, Massachusetts Institute of Technology, Cambridge, MA, USA; McGovern Institute, Massachusetts Institute of Technology, Cambridge, MA, USA; Howard Hughes Medical Institute, Massachusetts Institute of Technology, Cambridge, MA, USA; Koch Institute, Massachusetts Institute of Technology, Cambridge, MA, USA; Center for Neurobiological Engineering, Massachusetts Institute of Technology, Cambridge, MA, USA.

[14] Department of Biotechnology and Biophysics, Biocenter, University of Würzburg, Am Hubland, 97074 Würzburg, Germany

[15] NanoTag Biotechnologies GmbH, Rudolf-Wissell-Straße 28a, 37079 Göttingen, Germany

*corresponding authors: ali.shaib@med.uni-goettingen.de; srizzol@gwdg.de

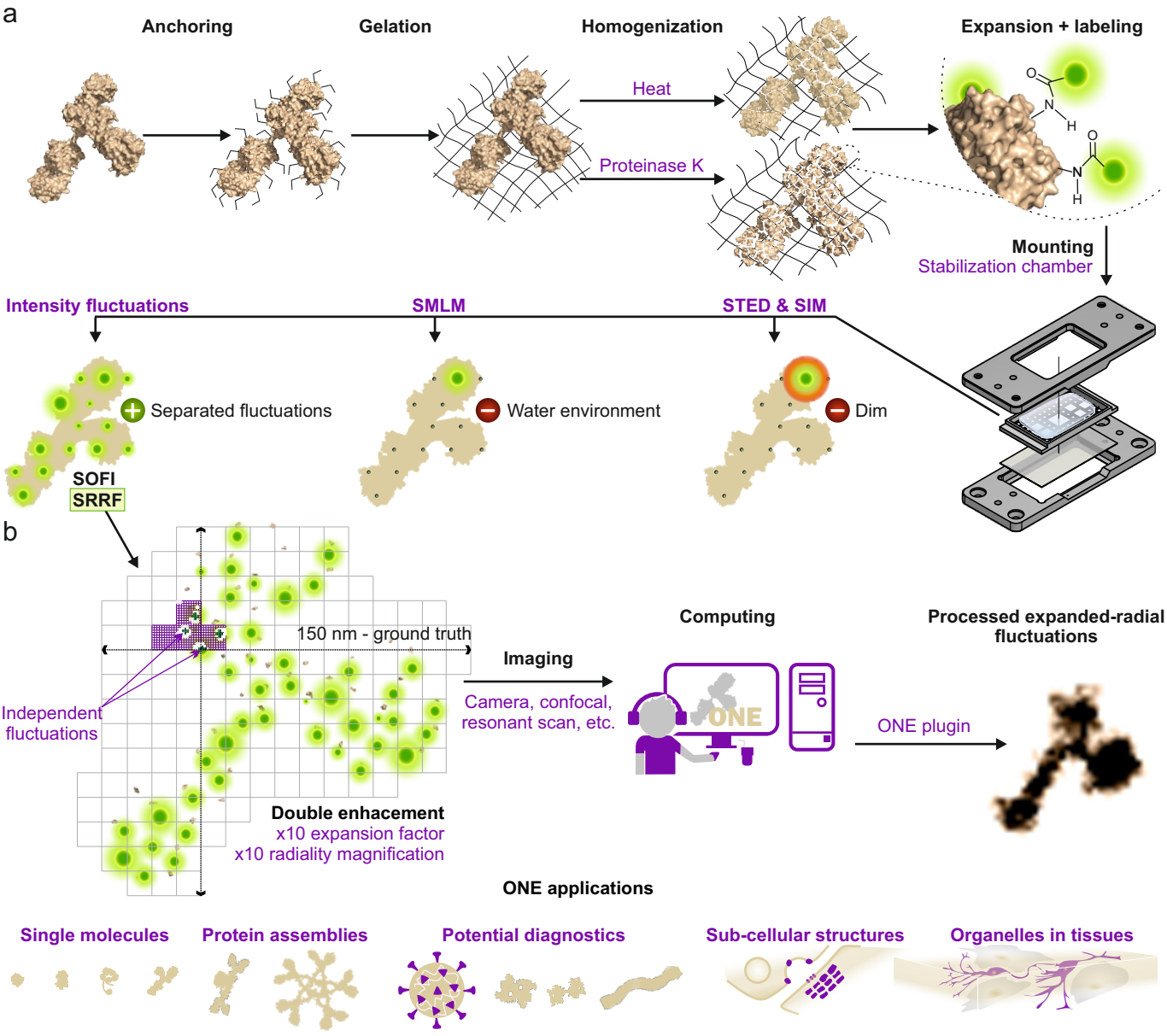

Extended Data Fig. 1. A general overview of the ONE microscopy approach. a, Biological samples are linked to gel anchors, relying on Acryloyl-X, followed by X10 gel formation and homogenization, either by proteinase K additions or by autoclaving in alkaline buffers. Full expansion is achieved by repeated washes, and is followed by mounting gel portions in a specially designed chamber. In principle, one could image the samples using different super-resolution procedures. Techniques benefitting from bright samples, as STED or SIM, suffer due to the fluorophore dilution induced by the expansion procedure. Techniques requiring special buffers (e.g. SMLM) are negatively affected by the water environment. In contrast, technologies relying on fluorophore fluctuations profit from the expansion, as the fluorophores are spatially separated and can fluctuate independently. **b**, Repeated imaging is performed (up to 3000 images), in any desired imaging system (confocal, epifluorescence, etc.), to detect signal fluctuations, which are then computed using through a plugin (ONE platform) based on the SRRF algorithm, before assembling the final super-resolved images.

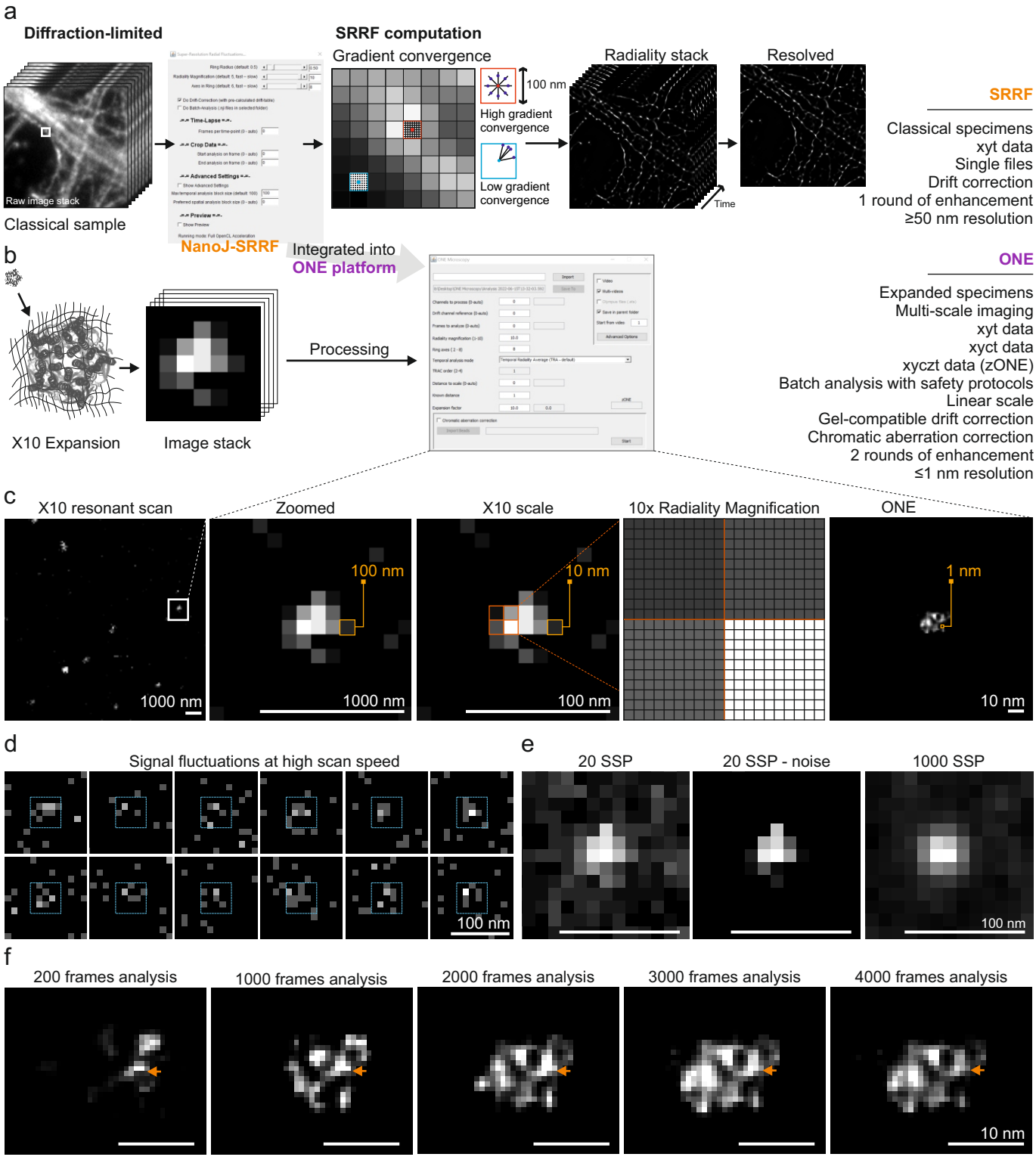

Extended Data Fig. 2. A detailed view of the ONE procedure. a, Processing a stack of diffraction-limited images with SRRF, based on the analysis of a gradient of convergence of sub-pixels over a radiality stack, results in super-resolved images with resolutions varying between 50-70 nm. **b**, The ONE procedure adapts the SRRF algorithm to expanded gels. c-f, A detailed explanation of the analysis procedure. **c**, A sample was fixed and expanded using a 10-fold expansion protocol (X10). The sample was then imaged using a resonant scanner on a confocal microscope. The zoomed-in view indicates one bright spot, whose size in real space is limited by diffraction to ~200-300 nm, but represents a 10-fold smaller size in the pre-expansion space (see scale bars in the middle panels). Every pixel is then subjected to a 10-fold radiality magnification and is then subjected to the procedure explained in panels **d-f**, which provides the final, high-resolution image (right-most panel). d, Signal fluctuations are measured by imaging the sample repeatedly, using the resonant scanner (here at 8 kHz). **e**, A view of the overall signals, obtained by summing 20 of the fluctuating images (raw in the left-most panel, background-subtracted in the middle panel), or by summing 1000 images. **f**, Each image from series obtained as in panel b is subjected to a temporal analysis of fluctuating fluorophores, based on radiality magnification[6], thereby providing a super-resolved image whose level of detail becomes optimal after ~1500 frames.

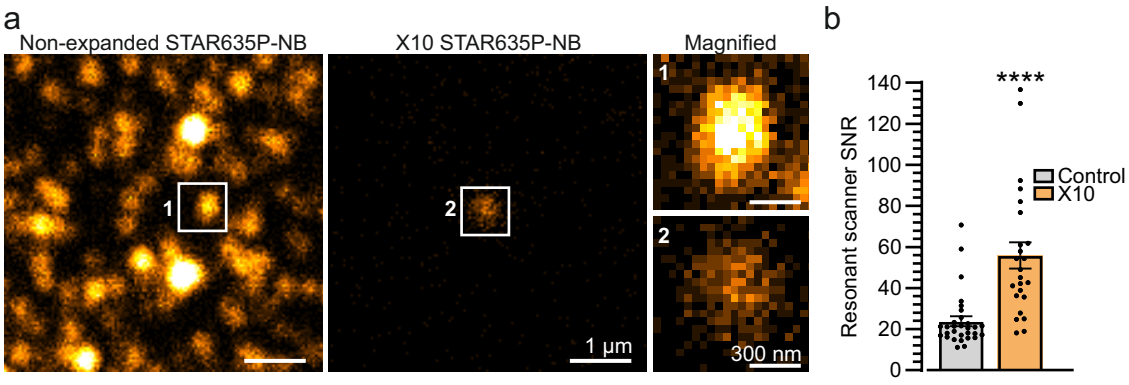

Extended Data Fig. 3. Expansion microscopy results in a higher signal-to-noise ratio. Expansion microscopy, which separates proteins of interest and removes much of the other cellular components (e.g. lipids, metabolites) should result in a higher signal-to-noise ratio (SNR). **a**, To test this, we analyzed here the simplest possible sample, consisting of Star635P-conjugated nanobodies on glass coverslips, or in expanded gels, using confocal microscopy, relying on analysis using a resonant scanner. **b**, The SNR of these samples increases by 2-fold, on average, after expansion. N = 30-24, P = 0.000001, Mann-Whitney Ranksum test.

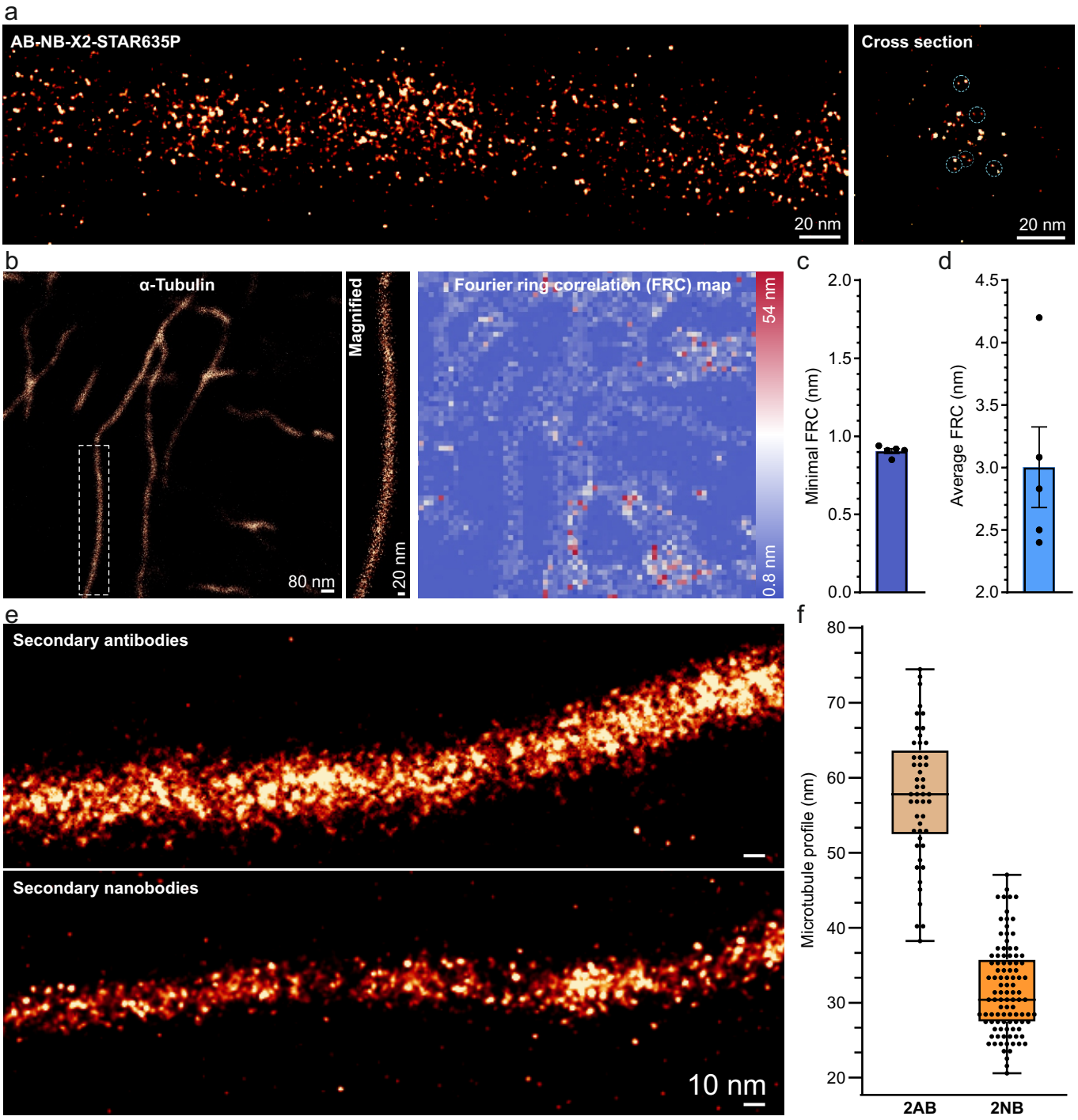

Extended Data Fig. 4. The ONE resolution reaches sub-nanometer values in tubulin immunostainings. a, An analysis of tubulin, following immunostainings relying on primary antibodies detected using Star635P-conjugated secondary nanobodies. While the overall signal distribution is similar to that obtained with secondary antibodies (Fig. 1), one can observe often pairs of fluorescent spots in very close vicinity (marked by dotted circles in the cross section), which probably represent the two fluorophores on each nanobody. For a formal analysis of this issue on different nanobodies, see Fig. 1 and Extended Data Fig. 5. **b**, A Fourier Ring Correlation (FRC) analysis of a tubulin immunostaining. The best resolution obtained is ~0.8 nm. **c**, The best resolution obtained per image (N = 5 analyses). **d**, The average resolution obtained per image (N = 5 analyses). **e**, Immunostainings relying on primary antibodies followed by secondary antibodies (upper panel) or by secondary nanobodies (lower panel). **f**, The graph shows the diameter of microtubules in when using secondary antibodies (left; N = 49 microtubule profiles) or secondary nanobodies (right; N = 101).

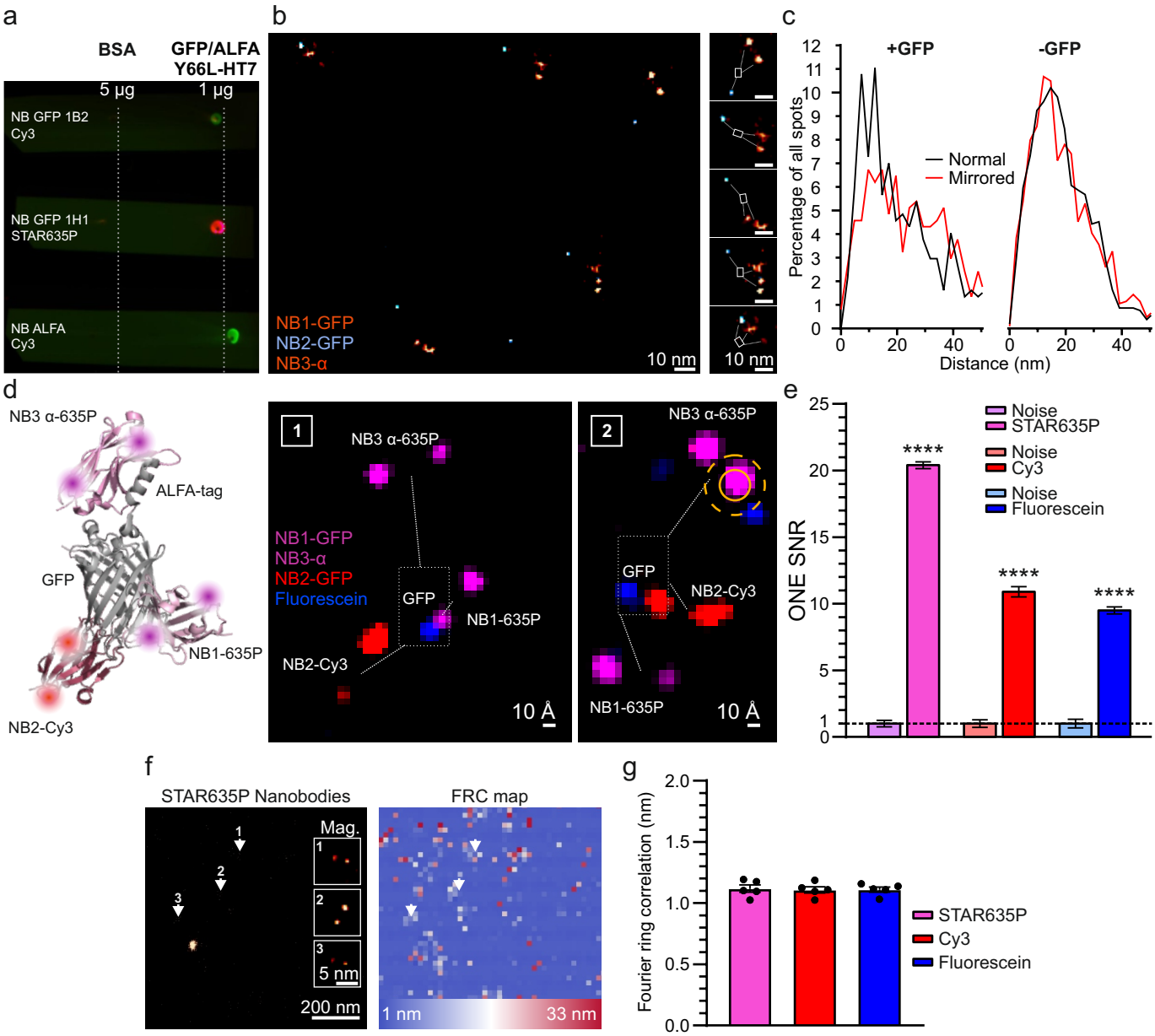

Extended Data Fig. 5. In-depth analysis of GFP-nanobody complexes. a, Dot blots to validate that each nanobody was binding specifically the TSR individually. Nitrocellulose membranes were spotted with TSRs and bovine serum albumin, as control, and the spots were revealed with the respective nanobodies. **b**, An overview of an image showcasing nanobodies bound to their GFP target. **c**, An analysis of distances from STAR635P to Cy3 nanobodies, in normal images or after mirroring one of the fluorescence channels, as a negative controls. The close-distance interval is largely removed by mirroring. N = 40-40 TSRs. Performing this in samples lacking the GFP, in which the nanobodies are randomly distributed, results in no differences between the normal and mirrored distributions. N= 40/40 images. **d**, Overview of the TSR using only two-color nanobody labeling (same as the one used in Fig. 5c,d), along with two different examples. The sample is also labeled using NHS-ester fluorescein, and a small pixel size (0.48 nm) is used, to enable the optimal visualization of the TSRs. **e**, An analysis of the signal-to-noise ratio of the TSRs, obtained by measuring the noise levels in the vicinity of the nanobodies. The noise levels are normalized to 1, implying that the normalized signal of the respective nanobodies now provides directly the signal-to-noise ratio. N = 20-18, 12-14, and 17-11 measurements, $p < 0.0001$, Mann-Whitney test. **f**, A Fourier Ring Correlation (FRC) analysis of nanobody images. The best resolution obtained is ~1 nm. **g**, The best resolution obtained per image, in the different color channels (N = 5 analyses).

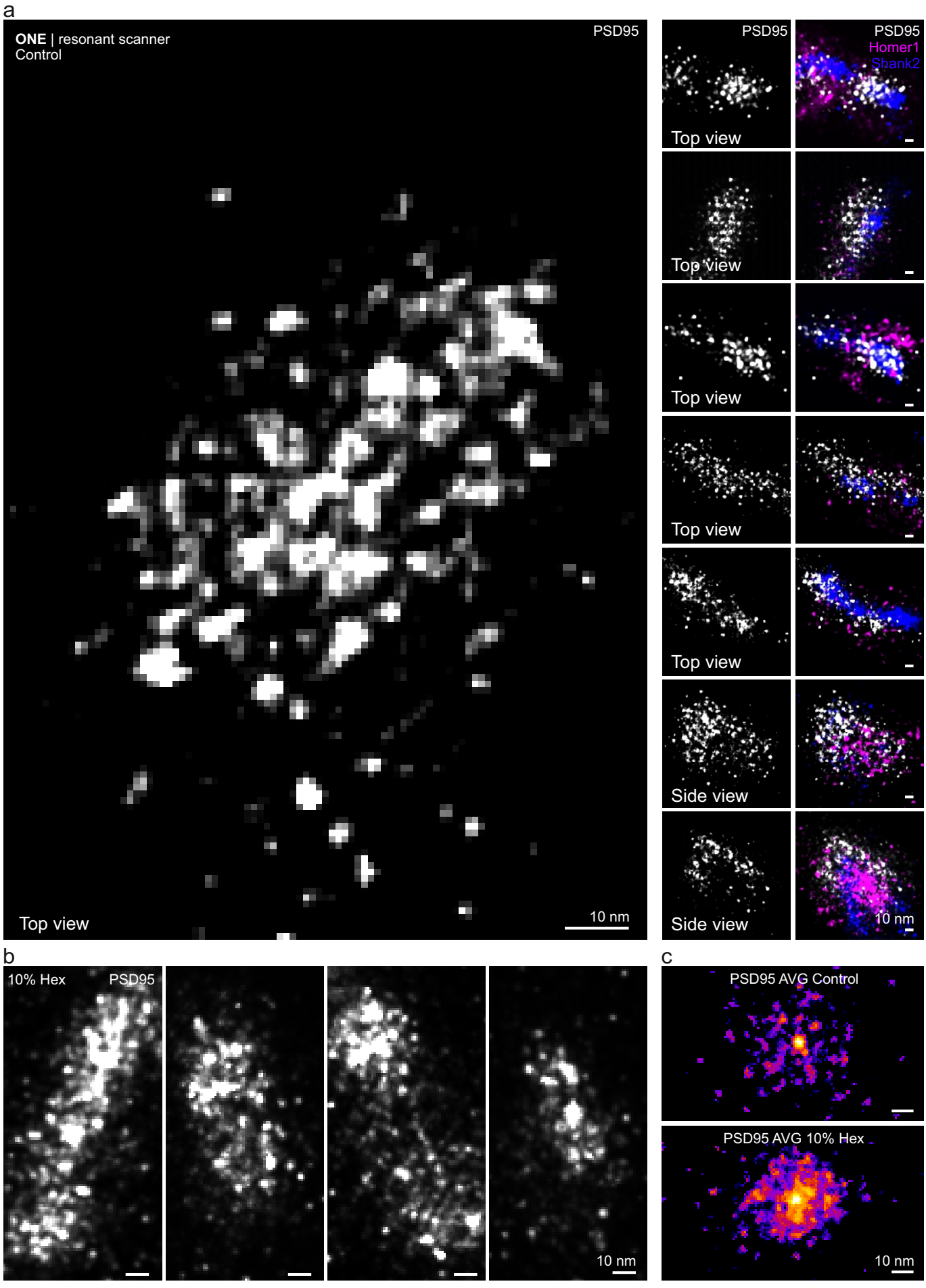

Extended Data Fig. 6. Further PSD examples. a, ONE imaging of PSDs, employing a resonant scanner and a final pixel size of 1 nm, achieving high resolution (same procedure and resolution as in Fig. 3f). **b**, Examples of PSD95 stainings, after treatment with 1,6-hexanediol (Hex), as in Fig. 3f. **c**, We averaged the PSD95 signals for both control and Hex-treated synapses (8 PSDs imaged in top views, for each treatment). The control shows a somewhat regular pattern, while the Hex treatment seems to perturb this.

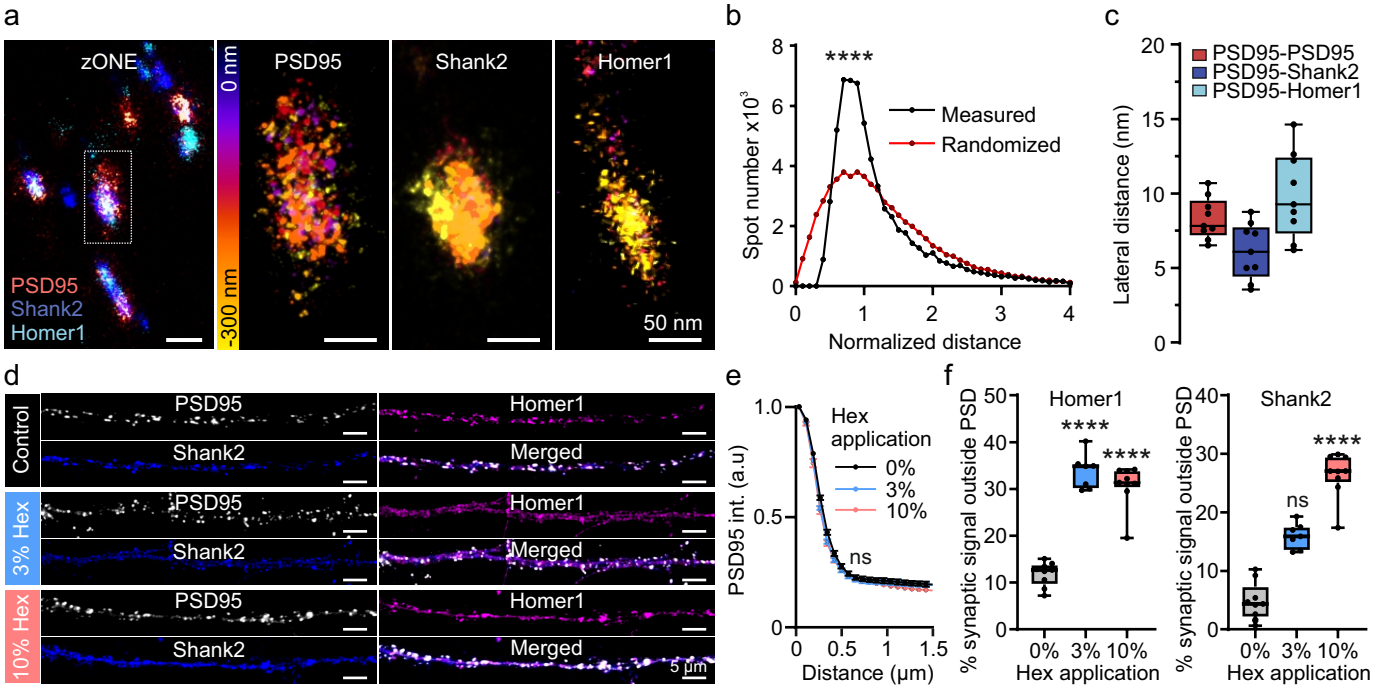

Extended Data Fig. 7. A detailed analysis of the PSD. a, The PSD was immunostained for PSD95, Homer1 and Shank2, as in Fig. 3, and images were taken at different heights along the Z-axis (zONE imaging). An overlay (summed image) is shown in the left panel, along with an analysis of the proteins at different Z levels, using a colormap that describes the positions along the Z axis (right panel). **b**, The distance between PSD95 spots was computed from images as in panel a, and was compared to that obtained from positioning the molecules randomly within the PSD95, N = 10 synapses, Friedman test followed by Dunn-Sidak, p=0.0001. **c**, The lateral distance between PSD95 spots and between PSD95 and Homer1 or Shank2. The minimal distance between each PSD95 spot and a Homer1/Shank2 spot is shown (measured in the lateral plane, in 2D projections of the PSD). N = 10 synapses, from 2 independent experiments. While the distance between PSD95 spots has a non-random character, as indicated in panel b, the distances to Homer1 or Shank2 spots are not different from randomized distributions (Dunn-Sidak tests, p > 0.1), possibly also because these two molecules are immunostained using antibodies, which causes the fluorescence signals to scatter broadly. **d**, Confocal microscopy analysis of the PSDs, in non-expanded samples. In control conditions all three components analyzed here (PSD95, Homer1, Shank2) are well colocalized. The addition of 3% 1,6-hexanediol (Hex) causes the dispersion of Homer1 (magenta), while 10% Hex also disperses Shank2 (blue). PSD95 remains largely unaffected by Hex. **e**, An analysis of the average PSD95 spot profile confirms this impression, N = 10-7-10 neurons, a set from 3 independent experiments. f, We analyzed the dispersion of Homer1 (left) and Shank2 (right) away from the PSD95 spots. The signal present in synapses (near the PSD95 labeling, but not within the PSD) was analyzed, to determine the % that is not correlating to the PSD structure. The same samples were analyzed as in panel e.

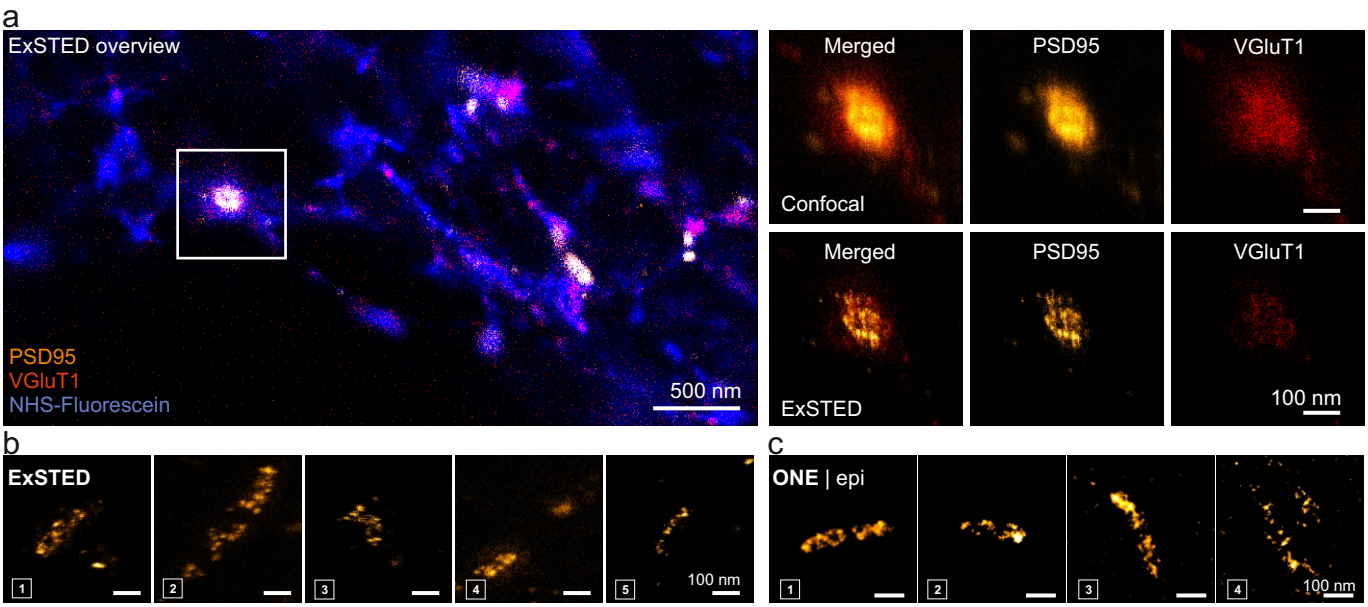

Extended Data Fig. 8. ExM-STED (ExSTED) imaging of PSDs. a, Hippocampal cultures were immunostained for PSD95 and VGlut1, and were additionally labeled with NHS-ester fluorescein, after homogenization. **b**, A gallery of high-zoom ExM-STED views of synapses, with a focus on PSD95. Relatively large PSD domains are visible, as in most previous works in the literature, and unlike most of our ONE images. **c**, To determine if this is simply an issue of resolution, we aimed to generate ExM-STED-like images with ONE microscopy, by reducing its resolution. We employed an epifluorescence microscope (as opposed to a rapidly scanning confocal in the panels dealing with PSD95 in Fig. 3), and we used the temporal radiality pairwise product mean (TRPPM) option of analysis, which broadens the resulting spots. The results are very similar to ExM-STED images, demonstrating that the modular/ domain appearance of the PSD95 stainings is a result of insufficient resolution, with a retiolum being evident only at very high resolution (under optimal ONE imaging).

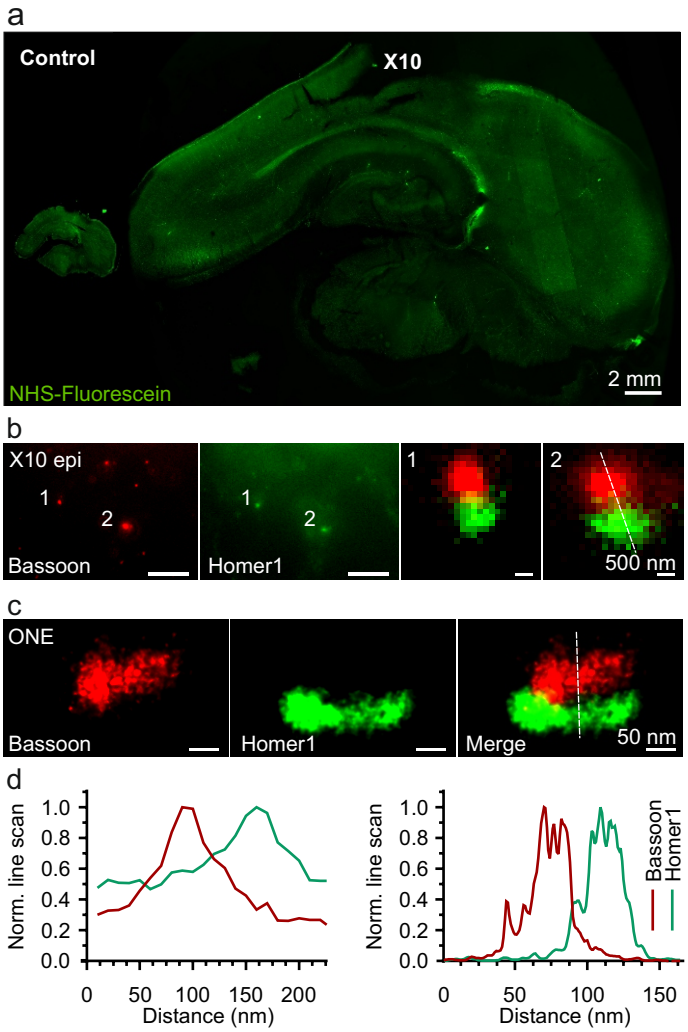

Extended Data Fig. 9. ONE analysis of brain slices. a, Images of a 200 µm-thick rat brain section before (left) and after (right) expansion, relying on autoclaving for homogenization69. The scale bar does not take the expansion factor into consideration. The sections were labeled by using NHS-ester fluorescein incubations. **b**, Epifluorescence images of expanded brain slices, focusing on Bassoon and Homer1 as pre- and postsynaptic markers, respectively. **c**, Similar images, taken using the ONE procedure. **d**, Line scans executed over the areas indicated in panels b and c. As expected, far more detail can be observed in ONE than in simple epifluorescence microscopy.

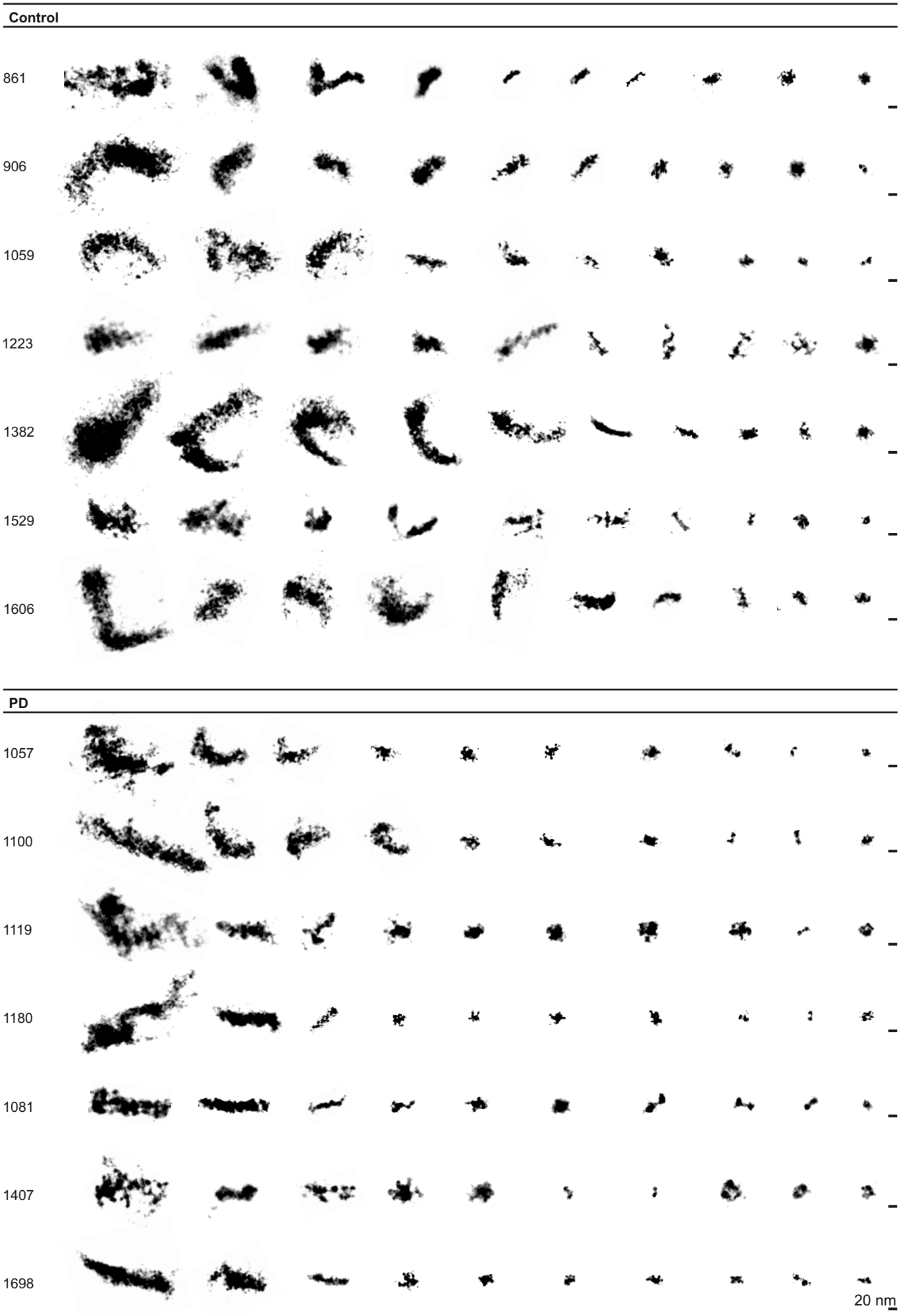

Extended Data Fig. 10. A gallery of ASYN object images from 7 PD patients and 7 controls. The images were obtained following the procedure indicated in Fig. 4a. See Supp. Table 1 for details on the respective patients.

Supplementary Figures

Expansion microscopy at one nanometer resolution

Ali H. Shaib[1,*], Abed Alrahman Chouaib[2], Vanessa Imani[1], Rajdeep Chowdhury[1], Svilen Veselinov Georgiev[1], Nikolaos Mougios[1,3], Mehar Monga[4], Sofiia Reshetniak[1], Daniel Mihaylov[5], Han Chen[6], Parisa Fatehbasharzad[1], Dagmar Crzan[1], Kim-Ann Saal[1], Claudia Trenkwalder[7,8], Brit Mollenhauer[8,9], Tiago F. Outeiro[10], Julia Preobraschenski[4,11], Ute Becherer[2], Tobias Moser[6,11,12], Edward S. Boyden[13], A Radu Aricescu[5], Markus Sauer[14], Felipe Opazo[1,3,15], Silvio O. Rizzoli[1,3,11,*]

[1] Institute for Neuro- and Sensory Physiology, University Medical Center Göttingen, Göttingen, Germany

[2] Department of Cellular Neurophysiology, Center for Integrative Physiology and Molecular Medicine (CIPMM), Saarland University, Homburg, Germany

[3] Center for Biostructural Imaging of Neurodegeneration, University Medical Center Göttingen, Göttingen, Germany

[4] Biochemistry of Membrane Dynamics Group, Institute for Auditory Neuroscience, University Medical Center Göttingen, Göttingen, Germany

[5] MRC Laboratory of Molecular Biology, Cambridge, UK.

[6] Institute for Auditory Neuroscience and InnerEarLab, University Medical Center Göttingen, Göttingen, Germany

[7] Department of Neurosurgery, University Medical Center, Göttingen, Germany

[8] Paracelsus-Elena-Klinik, Kassel, Germany

[9] Department of Neurology, University Medical Center, Göttingen, Germany

[10] Department of Experimental Neurodegeneration, Center for Biostructural Imaging of Neurodegeneration, University Medical Center Göttingen, 37073 Göttingen, Germany; Max Planck Institute for Multidisciplinary Sciences, 37075 Göttingen, Germany; Translational and Clinical Research Institute, Faculty of Medical Sciences, Newcastle University, NE2 4HH, United Kingdom; Scientific Employee with an Honorary Contract at German Center for Neurodegenerative Diseases (DZNE), 37075 Göttingen, Germany

[11] Cluster of Excellence "Multiscale Bioimaging: from Molecular Machines to Networks of Excitable Cells" (MBExC), University of Goettingen, Göttingen, Germany

[12] Auditory Neuroscience and Synaptic Nanophysiology Group, Max Planck Institute for Multidisciplinary Sciences, Göttingen, Germany

[13] Department of Brain and Cognitive Sciences, Massachusetts Institute of Technology, Cambridge, MA, USA; Department of Biological Engineering, Massachusetts Institute of Technology, Cambridge, MA, USA; McGovern Institute, Massachusetts Institute of Technology, Cambridge, MA, USA; Howard Hughes Medical Institute, Massachusetts Institute of Technology, Cambridge, MA, USA; Koch Institute, Massachusetts Institute of Technology, Cambridge, MA, USA; Center for Neurobiological Engineering, Massachusetts Institute of Technology, Cambridge, MA, USA.

[14] Department of Biotechnology and Biophysics, Biocenter, University of Würzburg, Am Hubland, 97074 Würzburg, Germany

[15] NanoTag Biotechnologies GmbH, Rudolf-Wissell-Straße 28a, 37079 Göttingen, Germany

*corresponding authors: ali.shaib@med.uni-goettingen.de; srizzol@gwdg.de

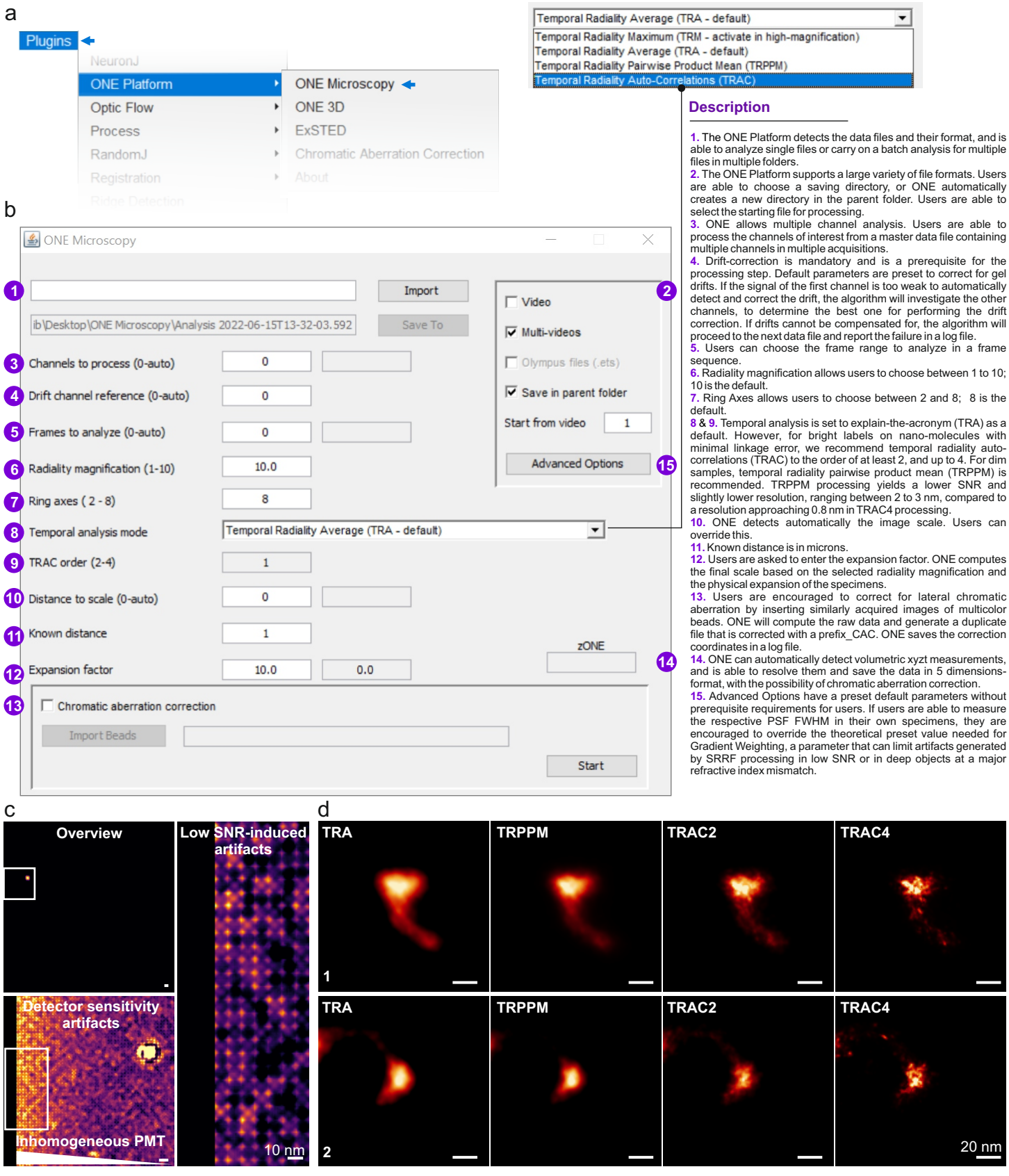

Supplementary Fig. 1. ONE analysis and examples. a & **b**, Several views of the starting interface of the ONE software package. The examples show the intuitive software choices. See also the “Readme/Help” file of the software package. **c**, Examples of different potential artifacts that should be avoided in ONE imaging. **d**, Different potential choices in how to resolve ONE images. We suggest using the TRPPM procedure for dim samples. This reduces the obtainable resolution, but follows much better the potential molecule shape. For brightly labeled samples with direct labeling, the TRAC4 procedure provides the best resolution and SNR, indicating the positions of the individual fluorophores.

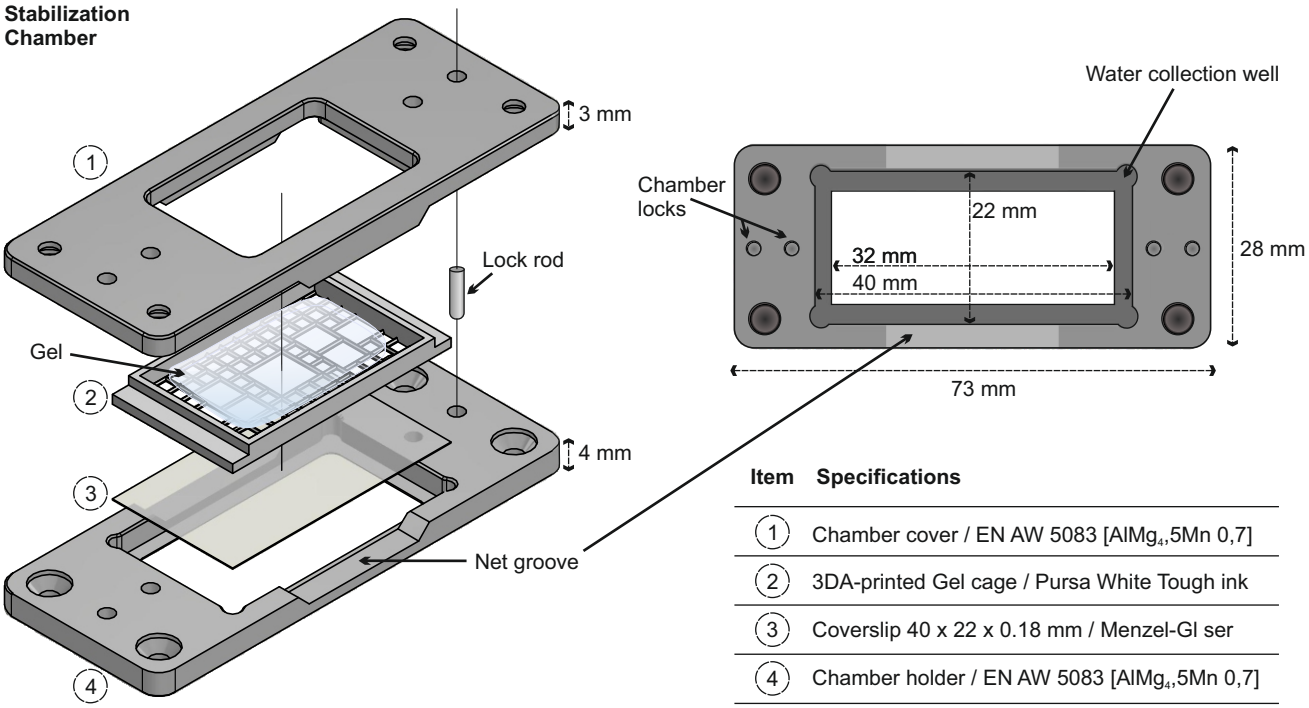

Item	Specifications
1	Chamber cover / EN AW 5083 [$AlMg_4$,5Mn 0,7]
2	3DA-printed Gel cage / Pursa White Tough ink
3	Coverslip 40 x 22 x 0.18 mm / Menzel-Gl ser
4	Chamber holder / EN AW 5083 [$AlMg_4$,5Mn 0,7]

Supplementary Fig. 2. Technical scheme of the stabilization chamber used in this work. The exact measurements and materials for the stabilization chamber are included in the figure text. The 3D-printed gel cage patterning can be organized according to the user's preferred design. Only a suggested design is included here (many others work equally well).

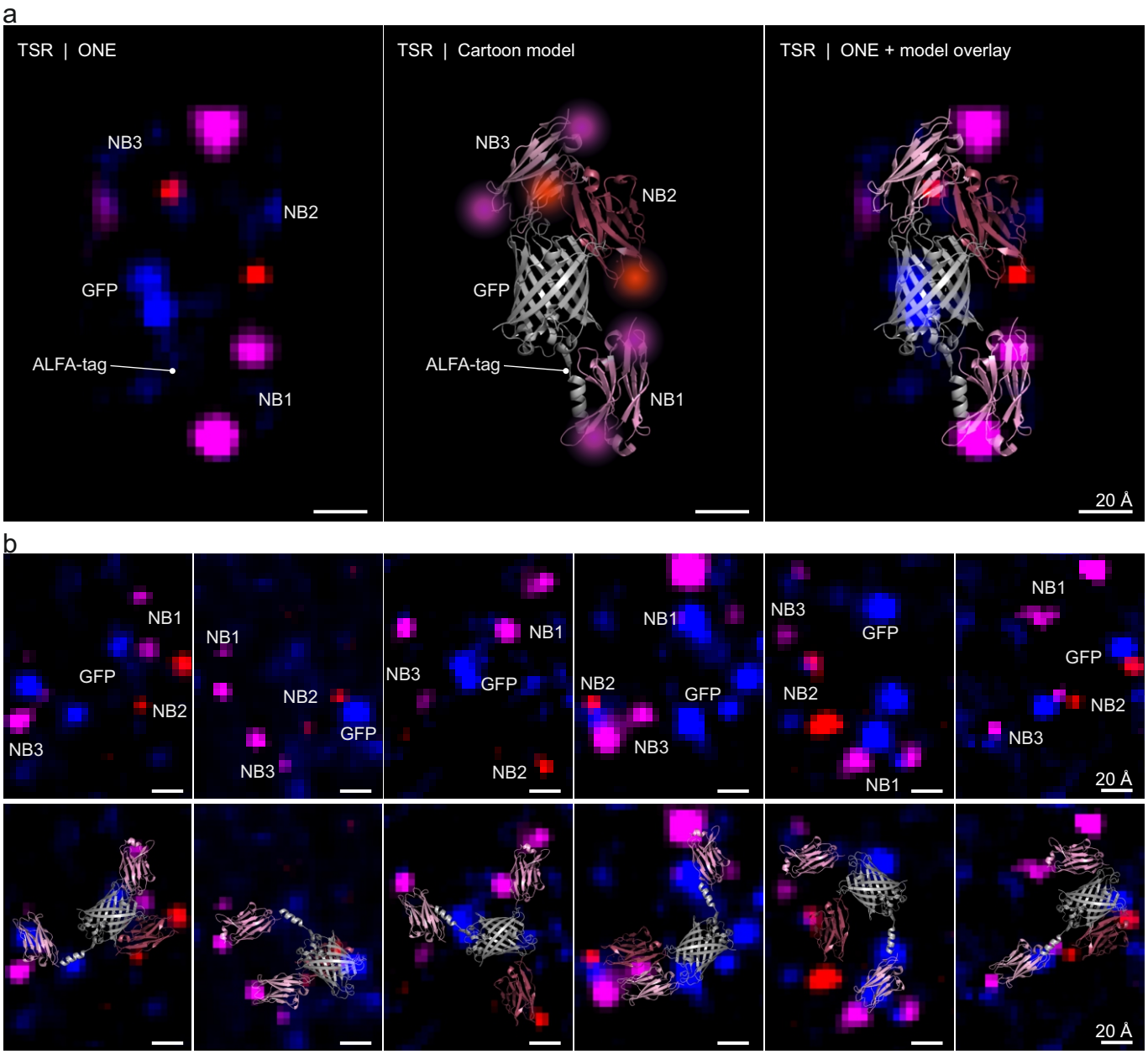

Supplementary Fig. 3. TSR gallery. a, An example of a TSR. The first panel shows a ONE image of a TSR, the middle panels shows a cartoon model that fits the imaged TSR, and the third panel shows an overlay of the ONE image and the model. **b**, A gallery of TSRs (upper panels) and a best guess of cartoon models overlaid over the TSR images (lower panels). The panels with cartoon overlays were generated using Pymol and Adobe Photoshop.

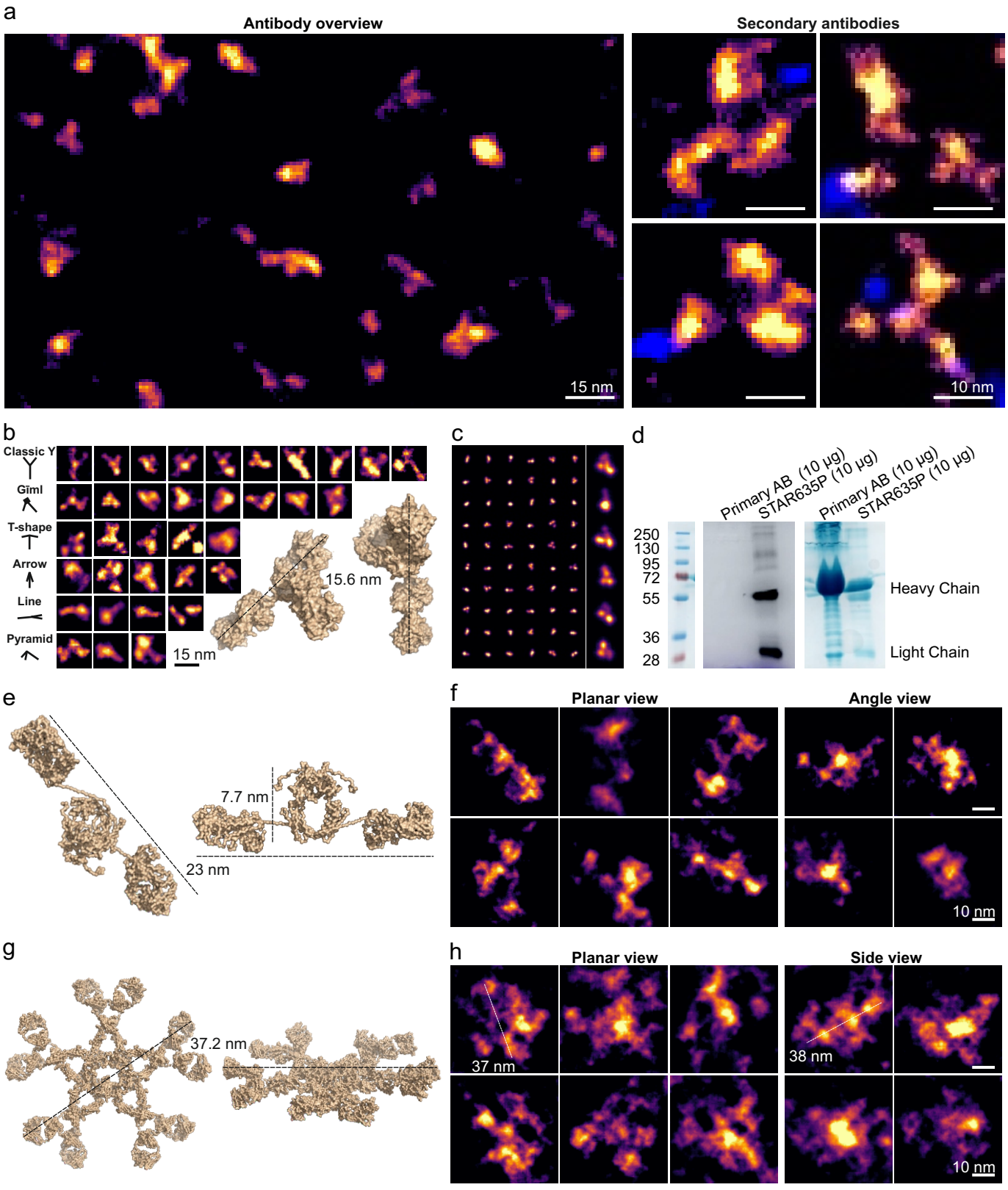

Supplementary Fig. 4. Further ONE examples of immunoglobulin imaging. a, An overview of a field showing IgG antibodies labeled using NHS-fluorescein (left), along with a few zoom-in images of fluorescently-conjugated secondary IgG antibodies (right; Abberior Star635P conjugation shown in blue). **b**, Several examples of IgG antibodies imaged in different positions and perspectives. **c**, A gallery of the expected antibody shapes, obtained by convoluting a PDB IgG structure with a ONE point-spread-function, after revolving the IgG molecules in 3D space randomly. A few enlarged views are shown, along with a multitude of small-sized views, to explain how IgG molecules should appear when they are visualized in fluorescence in random orientations. The typical IgG views are similar to the modeled ones. **d**, Fluorescence (Abberior Star635P) and Coomassie SDS-PAGE gels indicating the size distribution of antibody fragments. A mouse monoclonal primary antibody was run on the gels, along the secondary antibody imaged in panel a. The gel was first imaged under a fluorescence (Cy5 channel) and then total proteins were revealed with Coomassie brilliant blue staining. The results suggest that numerous small fragments are expected for both primary and secondary antibodies in the ONE images, not only full antibodies, due to impurities being present in the commercial antibody samples. **e-f**, An overview of IgA molecules. **g-h**, A similar overview of IgM molecules. The antibody structures are shown using Pymol representations from PDB structures 1HZH, 1IGA, and 2RCJ.

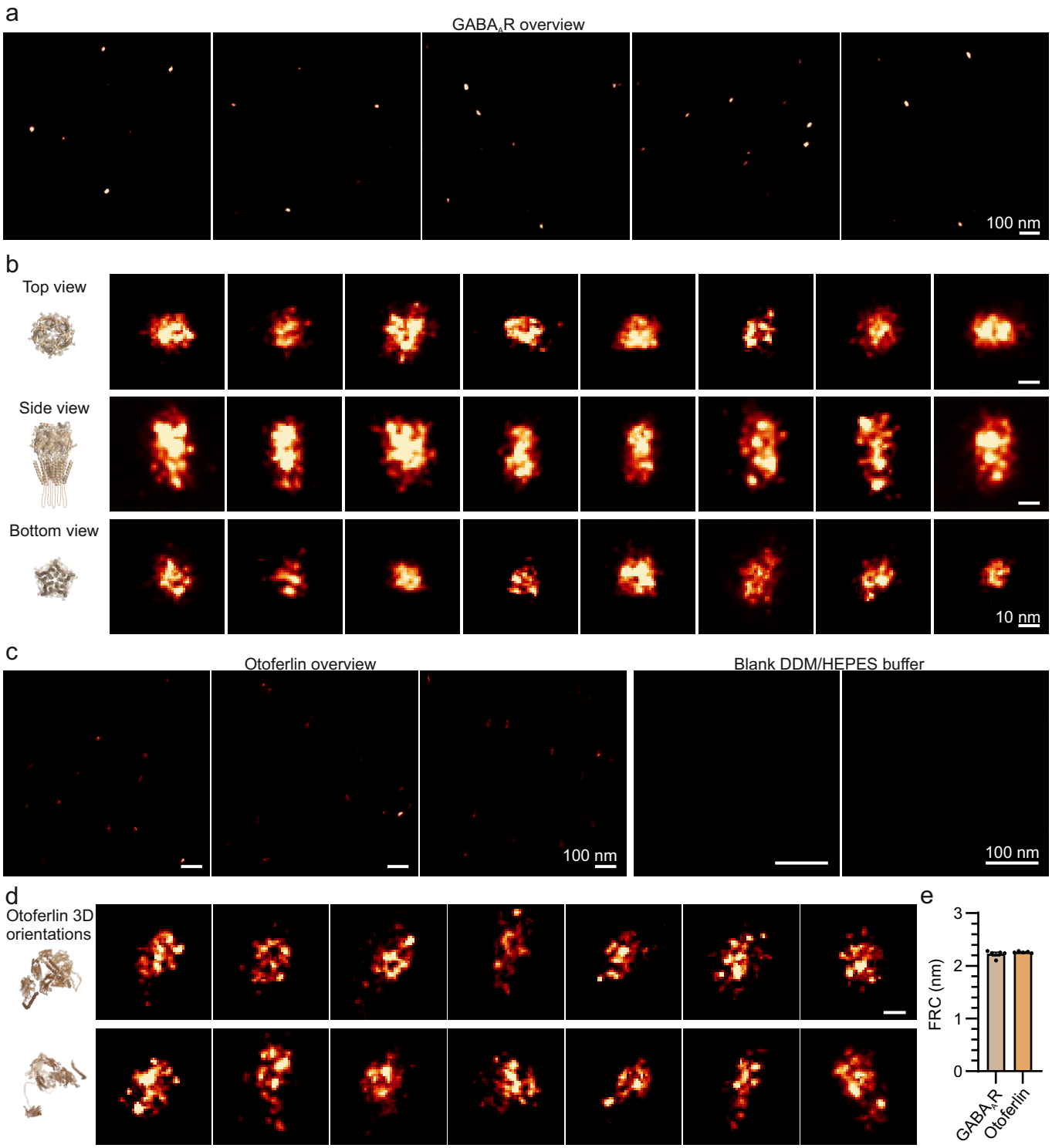

Supplementary Fig. 5. GABA$_A$ receptor and otoferlin galleries. a, An overview of images of GABA$_A$ receptors. **b**, The images display GABA$_A$ receptors in different 3D positions. The positional indications are best guesses performed by an experienced investigator. **c**, Overview images of otoferlin (right panel), and blank buffer as a control (left panel). **d**, Otoferlin images in different 3D positions. **e**, An FRC analysis of the resolution of such images indicates that the best resolution averages for GABA$_A$ receptors is 2.2 ± 0.03 nm (N = 5 analyses) and the best averages for otoferlin is 2.2 ± 0.007 nm (N = 5 analyses).

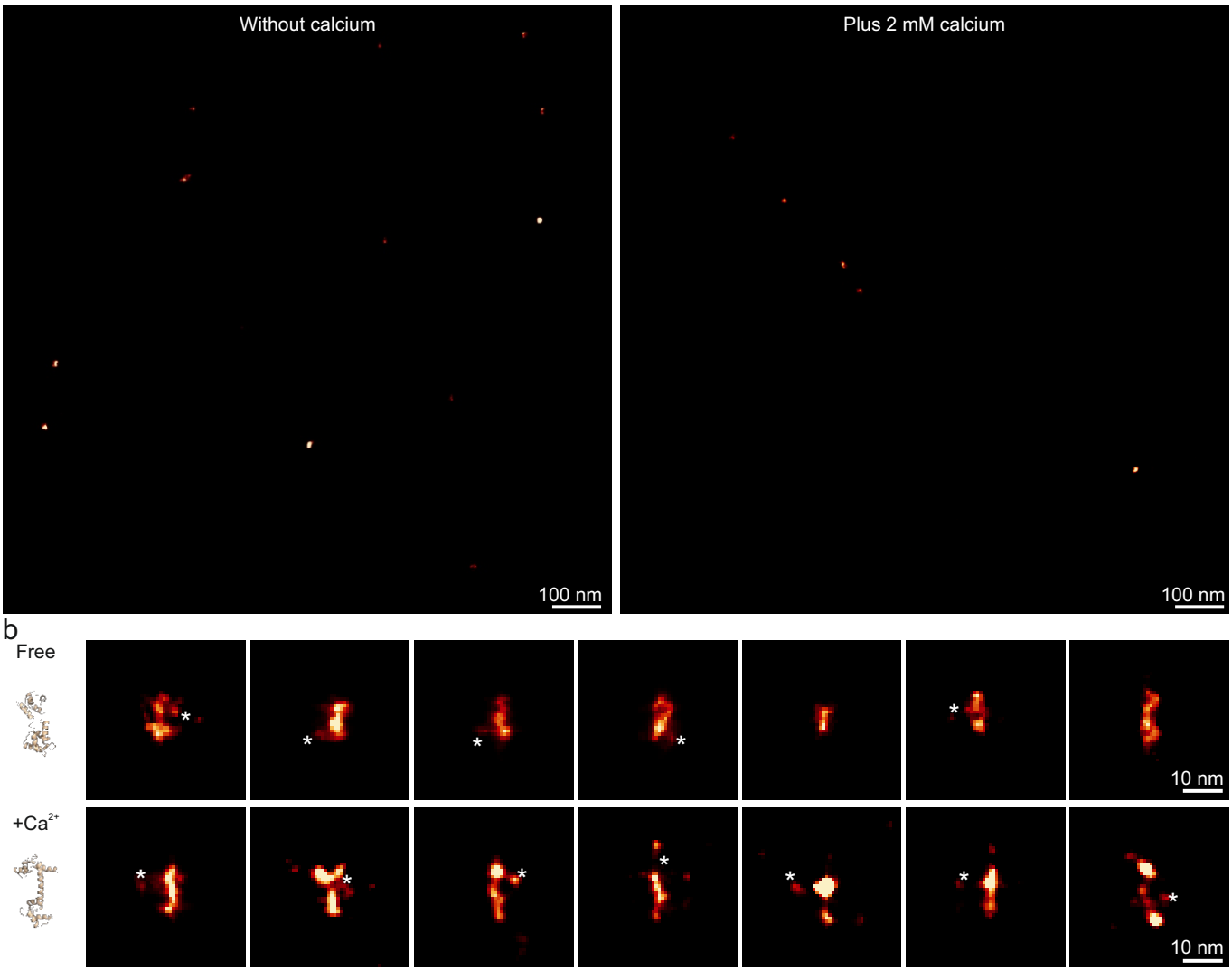

Supplementary Fig. 6. Calmodulin gallery. a, An overview of calmodulin ONE acquisitions in the presence and absence of calcium. **b**, Exemplary zoomed calmodulin ONE images. The asterisk denotes the best guess of GFP molecule bound to calmodulin.

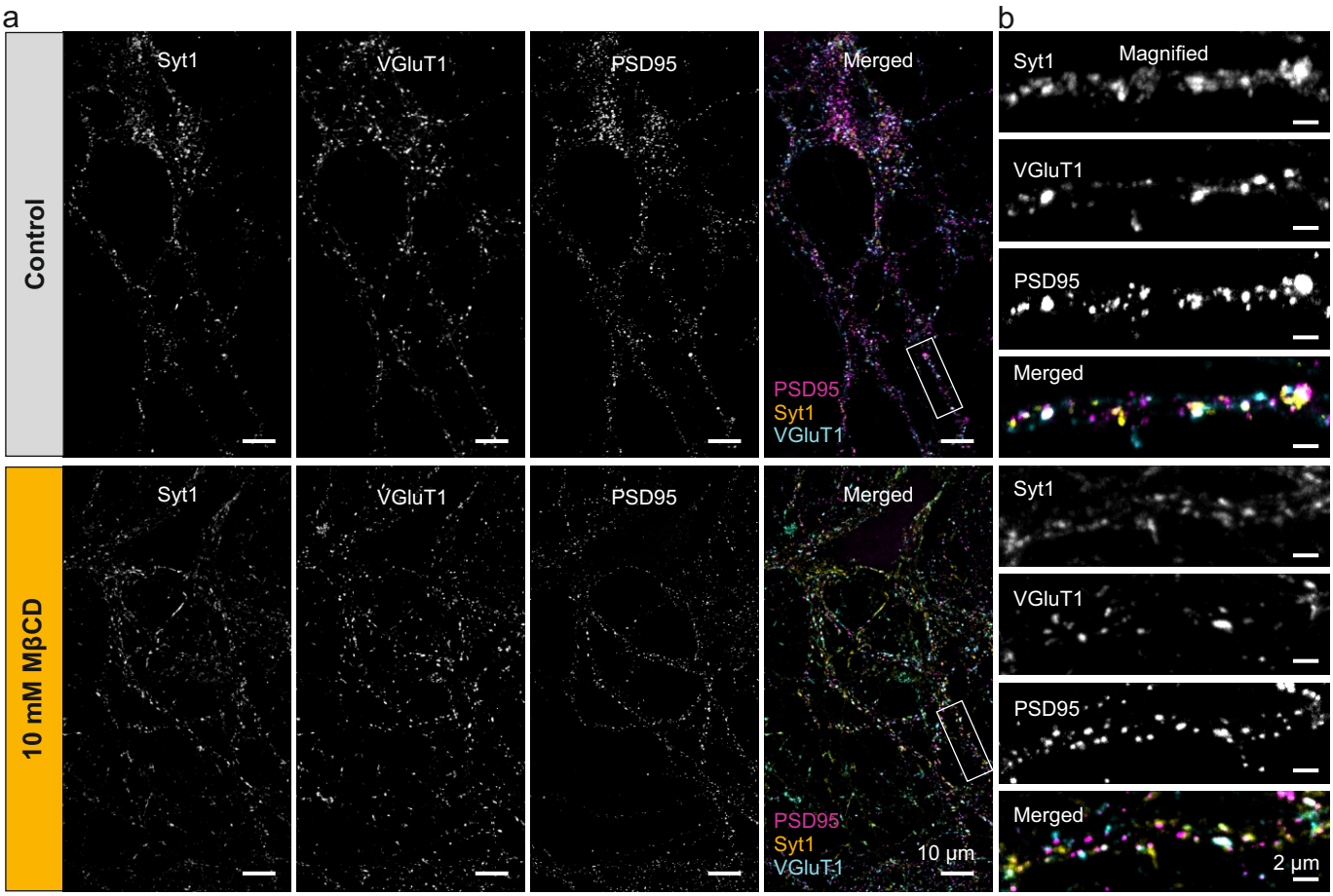

Supplementary Fig. 7. A confocal analysis of synapses after MβCD treatments. a, Confocal images of hippocampal cultures immunostained for the three synaptic markers employed in Fig. 3a-c (Syt1, vGlut1 and PSD95), relying on the same staining protocol as in Fig. 3a-c. **b**, The panels show a magnified region. The culture morphology and synapse distribution are similar before and after MβCD treatments.

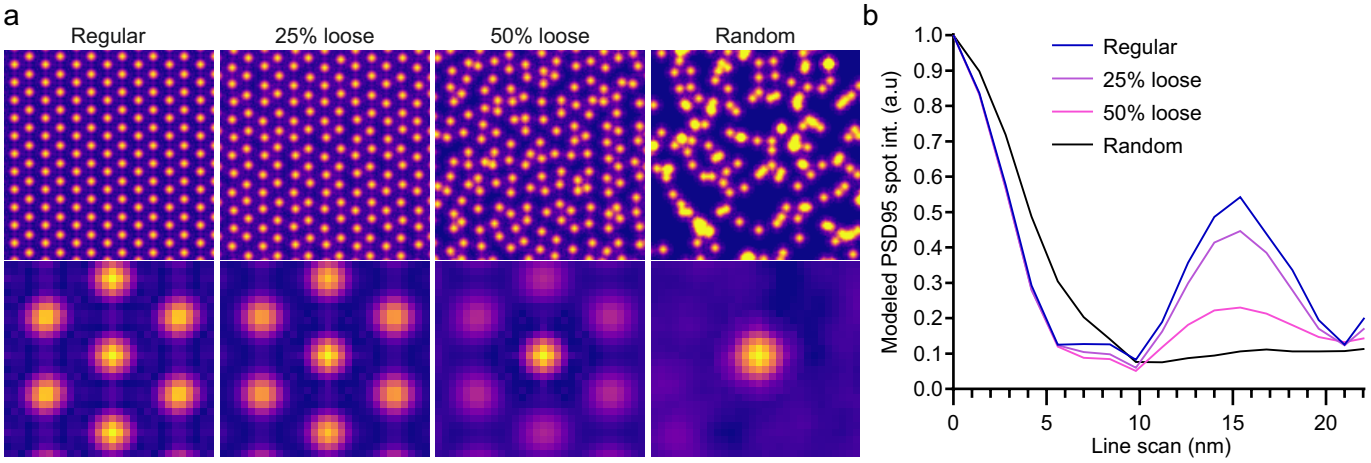

Supplementary Fig. 8. PSD95 model. a, To complement the distance analysis presented in Extended Data Fig. 7b, we analyzed the PSD95 distribution using a spot averaging procedure similar to a Ripley curve profile. To explain this analysis in more detail, we modeled it here. The top row of panels shows PSD-like spots, placed in a perfectly regular arrangement (left), with positions varying by 20 or 50% from perfect regularity (middle), or placed randomly (right). The bottom rows of panels show average spots, obtained by overlaying the areas surrounding each of the individual spots in the model arrangements from the top panels. This procedure results in arrangements in which the central spot is surrounded by increasingly weak spots, with virtually no regular spots around it in the right-most panel. **b**, Lines were drawn from the center of each spot in the bottom panels in panel a, in all directions, and were then averaged. The average line going from the center of a spot to the periphery shows a prominent peak if the arrangement is regular, since the neighboring spots are always present at a set distance, and thus provide a visible intensity peak. The less regular the arrangement is, the less clear the second peak becomes. It disappears completely when the spot positions are fully random.

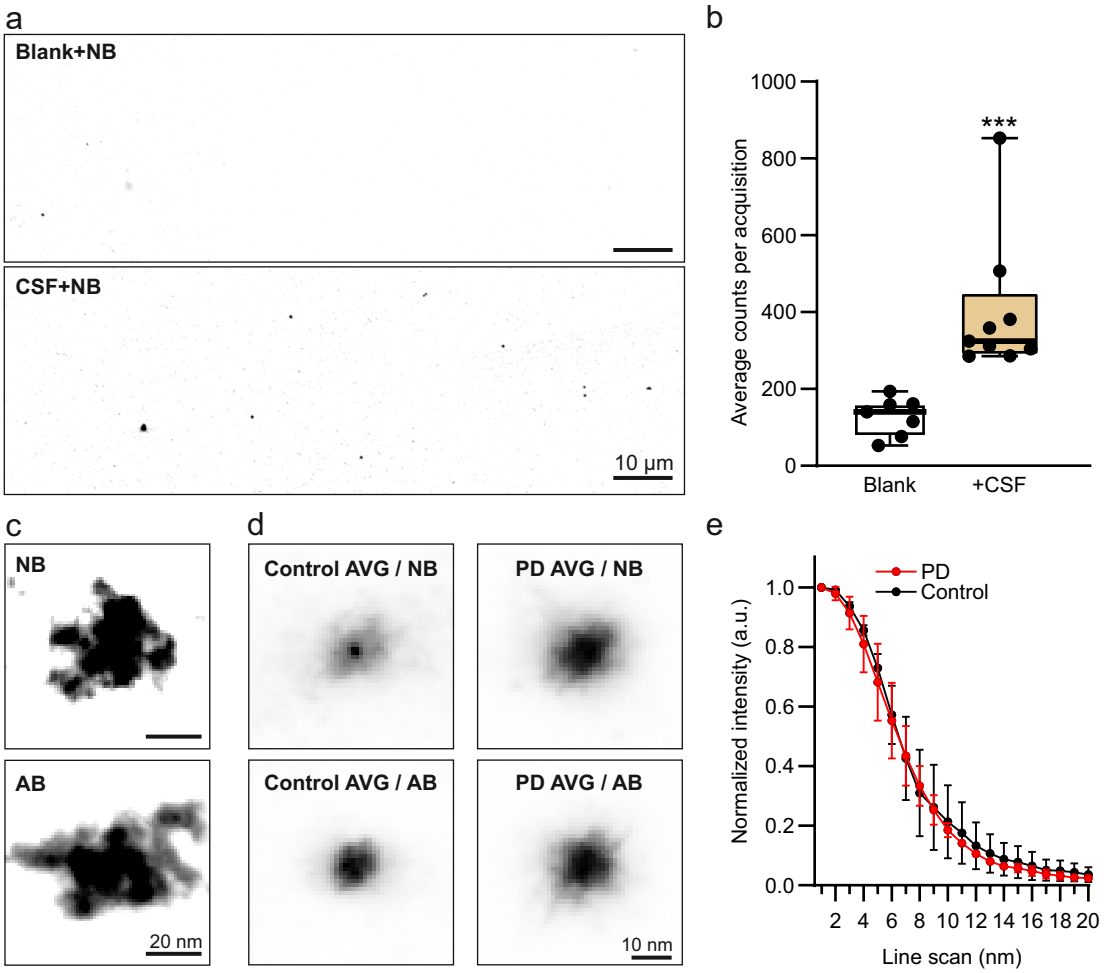

Supplementary Fig. 9. The nanobody imaging of ASYN objects is specific and is not easily reproduced by antibodies. a, Low-resolution images of CSF-containing samples, or blanks (clean, BSA-coated coverslips). Only a few dim spots, presumably representing single nanobodies, are seen in the blanks. **b**, Quantification of the signal intensity, as a sum across all image pixels. N = 7-9; Mann-Whitney test, P = 0.0002. **c**, Individual examples of oligomers immunolabeled with nanobodies (top) or antibodies (bottom). **d**, Averages of ASYN objects from individual patients, immunolabeled with nanobodies or antibodies. **e**, An analysis of the average object size in antibody-labeled samples, as in Fig. 4. N = 2 patients for each condition; the graph shows mean ± range of values. Nanobodies reveal differences between patients, at object sizes of only a few nm. Antibodies have difficulties in this direction, as their large size causes a lower-fidelity labeling, and as their sizes obscure the actual sizes of small objects.

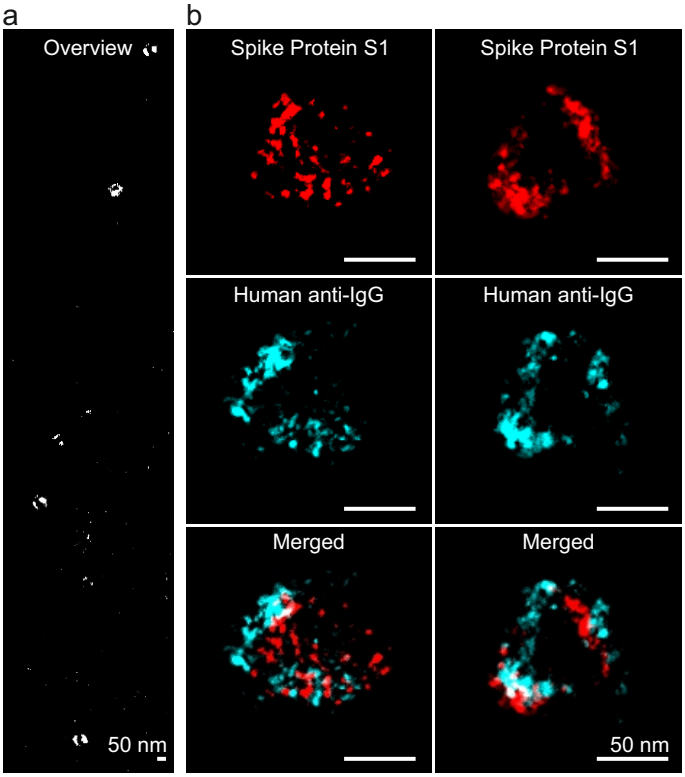

Supplementary Fig. 10. ONE analysis of SARS-CoV-2 viral particles. a, ONE overview of a sample containing SARS-CoV-2 viral particles immunostained against Spike Protein S1. **b**, More detailed views of two particles, indicating the Spike Protein S1 and the native IgG molecules from the serum of the patients. Interestingly, a domain-like structure is observed, which is presumably induced by the native IgGs gathering the spike proteins together, by the dual binding capacity of the IgG molecules.